On the Accuracy of Wireless Capsule Endoscope RF and Visual Localization

by

Mingda Zhou

A Thesis

Submitted to the Faculty

of the

WORCESTER POLYTECHNIC INSTITUTE

In partial fulfillment of the requirements for the

Degree of Master of Science

in

Electrical and Computer Engineering

by

May 2015

APPROVED:

Professor Kaveh Pahlavan, Major Thesis Advisor

Professor Yehia Massoud, Head of Department

”To whom I love, whom I learn from and whom I respect.”

Abstract

Wireless capsule endoscope (WCE) has become one of the most popular inspection devices which provides visual investigation of entire gastrointestinal (GI) tract. While the other traditional (wired) endoscopic devices are usually used for colon and stomach inspection. Locating abnormalities such as tumors, polyps and bleedings with wire-connected endoscope in GI tract is simple as long as we could measure the length of the wires inside human body. When WCE is applied, however, this becomes a critical challenge of examination since there is no wires connected to WCE while physicians need to find the exact locations of WCE to identify the position of abnormalities. To locate the WCE accurately, methods have come up in last decade including time of arrival (TOA) based methods, received signal strength (RSS) based methods, phase difference of arrival (PDOA) based methods, electromagnetic methods and video-based tracking methods, etc.. In this thesis, the accuracy of TOA, PDOA and video based localization methods are analyzed. (1) We propose a novel video-based tracking technique based on maximum mutual information, which provides a more accurate measurement of the displacement and rotation of the WCE inside the large intestine. (2) We derive the Cramer-Rao lower bound (CRLB) of TOA ranging using a single tone inside homogeneous tissues to examine the accuracy of three TOA ranging techniques. Then we compare the accuracy of these ranging techniques in non-homogeneous tissues with that in homogeneous tissues. (3) We also apply PDOA based ranging technique exploiting phase difference of two signals. Since the phase difference is taken into consideration, the ranging ambiguity of single tone is eliminated. We evaluate the accuracy of the proposed PDOA ranging technique and compare with that of TOA techniques.

Acknowledgements

First, I would like to express my deepest gratitude and respect to my advisor Kaveh Pahlavan, who guides me to the research field, who provides me the chance to take a glimpse of the world of engineering and who keeps sharing his sagacious tips on life and research. He is always generous on giving wise advises and helping me out when I encountered difficulties in my research. It is my honor to spend two years studying in CWINS Lab and to have him as my research advisor.

I am grateful to have Professor Xinming Huang, Professor Agu Emmanuel, Dr. Allen Levesque, and Dr. Steve Howard to be my committee members. Thank you for the priceless comments and reviewing of this thesis. And I would like to express my special thankfulness to Dr. Guanqun Bao, a former PhD student in CWINS Lab, for his constant help and support during my Master's study. Guanqun provided me with so many valuable suggestions and guided me as a co-author in most of my papers. Special thanks to Professor Huang, for his mental and financial support so that I could continue my PhD degree in WPI. Special thanks to Yishuang Geng and Bader Alkandari, for their patient guide and providing abundant resources for my research.

I also would like to say thanks to former and current members in CWINS Lab: Guanxiong Liu, Dr. Dan Liu, Dr. Shihong Duan, Yang Zheng, Chao Ren, Luyao Niu, Julang Ying, Yingyue Fan, Zhouchi Li, Yuzhang Zang, Yang Yang, Nader Bargshady and Dr. Yongtao Ma. Thank you so much for offering me a friendly yet active atmosphere in the lab, which is like a big family.

Finally, I would like to say that I owe my family. I cannot finish my Master's study without the support and believe from my parents, they always stand on my side when I was frustrated or depressed, even though they know little about what I am doing exactly. I thank my fiancee Xiaoxi Li, for her long-lasting support and unswerving love during the past years, and that would probably be extended to whole life.

Contents

List of Figures

List of Tables

List of Notations

Notation	Meaning
P_t	transmitted power
P_r	received power
c	speed of light
τ	time delay
$r(.)$	received signal
$s(.)$	transmitted signal
$\eta(.)$	background noise
N_0	spectral height of two sided noise
ω_c	angular frequency of signals
E_s	energy of transmitted signal
$R(.,.)$	correlation function
ε_r	relative permittivity
T_o	time of obervation
W	system bandwidth
λ	wavelength
σ	variance of shadow fading
$\mathbf{F}$	Fisher information matrix
$I(.,.)$	mutual information of two variables
$p(.,.)$	joint probability distribution
$H(.)$	Shannon entropy

Chapter 1

Introduction

In recent years, the rasing standardization of wireless body area networks (WBAN), IEEE 802.15.6 [1], aiming at providing a low power, short range and reliable wireless communication [2], brings new inspirations to health care [3]. Wireless capsule endoscope (WCE) is one of the most popular applications related to health care in WBAN. WCE is a swallowable medical device at pill size that carries a light source and camera as well as RF components. The WCE is first swallowed by a patient and then keeps taking pictures while travelling through the patient's gastrointestinal (GI) tract. At the same time, WCE transmits images outside the body which can be downloaded to help with the examination of GI tract. By reviewing the received images, physicians could detect the abnormalities and determine the severeness of those abnormalities.

1.1 Motivation

Even though the WCE indeed helps physicians detect the type and size of abnormalities [4], it does not prove sufficient knowledge about the exact location of abnormalities in the GI tract [5]. Different from wired endoscopy, wireless capsule endoscopy does not

have the wire connecting to exterior equipments, which makes it difficult to estimate the location. Thus, the accuracy needed for locating abnormalities inside GI tract becomes a critical and urgent issue [6].

To meet the challenges, some of the researchers proposed video aided WCE tracking algorithms to help physicians determine how the WCE moves inside small intestine [7] [8] [9]. Since little work has been done in large intestine, and the existing tracking algorithms in small intestine can not be utilized for the large intestine, an algorithm that helps tracking the WCE inside large intestine with high accuracy and stability is required.

Besides the video-aided motion tracking, time of arrival (TOA) localization is another way to locate the WCE. There is significant work using TOA-based technologies for localization inside the small intestine [10] [11] which applies first peak detection algorithm for the localization of WCE. More complex techniques used for estimating TOA, on the other hand, can potentially improve the performance of TOA localization, such as detection of all peaks, and etc.. Thus, test and analysis of these TOA estimation methods may help with the accuracy of TOA-based localization.

Further more, phase difference of arrival (PDOA) was designate for RFID indoor localization [12], but this technique can potentially be applied to localization inside human body. Since PDOA utilizes the difference of frequencies, it helps eliminate the ambiguity in WBAN, of which the TOA-based methods are not capable. Thus, investigation of PDOA localization is also important.

1.2 Contributions of the thesis

Being motivated by the description and to meet the above challenges, we propose a novel algorithm to improve the accuracy of WCE motion tracking and we also investigate TOA and PDOA methods to find out how we could make the in-body ranging more accurate,

both in homogeneous tissue and non-homogeneous tissues. The contributions of this thesis with three research directions in WCE localization are:

(a) Design of a novel approach to improve the accuracy as well as the stability of visual motion tracking of WCE inside the large intestine. Evaluation of our novel approach shows that the performance of our algorithm is capable to find the rotation angle and relative displacement of the WCE with acceptable errors throughout the entire process. Compared with other approaches, our approach also shows stable performance under all tested conditions. Detailed contribution to video motion tracking is reflected in:

1. Mingda Zhou, Guanqun Bao, and Kaveh Pahlavan. "Measurement of motion detection of Wireless Capsule Endoscope inside large intestine." Engineering in Medicine and Biology Society (EMBC), 2014 36th Annual International Conference of the IEEE. IEEE, 2014.

(b) Investigation of the accuracy of TOA-based ranging methods, including detection of the first peak, detection of all peaks and the generalized cross correlation coefficients. We compare their performance using finite difference time domain (FDTD) simulation in both homogeneous and non-homogeneous tissue with full body phantom. Analysis of the impact of non-homogeneity on the accuracy of TOA-based ranging methods are also performed. Detailed contribution to TOA-based ranging is reflected in:

2. Mingda Zhou and Kaveh Pahlavan, On the Accuracy of In-body TOA Ranging Inside the Gastrointestinal Tract Using Carrier Frequency, Wireless Telecommunication Symposium 2015, NYC, USA, April 15-17, 2015.

(c) Applying PDOA ranging method to in-body localization to expand the maximum ranging distance and analyze the performance of PDOA both with simulations and real measurements. We show that PDOA-based ranging does expand the maximum ranging distance, without obvious decrease of ranging accuracy. Detailed contribution to PDOA-

based ranging is reflected in:

3. Yongtao Ma, Mingda Zhou, Research of Phase of Arrival Based Ranging in Body Area Networks and Its Channel Modeling, Journal of Selected Area in Communication, IEEE, under review

Some other specific contributions of mine in this area are reflected by the list of publications below:

1. Mingda Zhou, Guanqun Bao, Yishuang geng, Bader Alkandari and Xiaoxi Li. "Polyp detection and radius measurement in small intestine using video capsule endoscopy." Biomedical Engineering and Informatics (BMEI), 2014 7th International Conference on. IEEE, 2014.

2. Guanqun Bao, Liang Mi, Yishuang Geng, Mingda Zhou and Kaveh Pahlavan, "A Video-based Speed Estimation Technique for Localizing the Wireless Capsule Endoscope inside Gastrointestinal Tract," the 36th Annual International Conference of the IEEE Engineering in Medicine and Biology Society (EMBC'14), Chicago, USA, August 26-30, 2014.

3. Dan Liu, Mingda Zhou, Yishuang Geng, Kaveh Pahlavan, Power Efficient Relay Networking for BANs in Non-Homogeneous Enviroment, IEEE WoWMoM, Bostong, USA, June 15-17, 2015, under review

1.3 Outline of This Thesis

This thesis primarily focus on the accuracy of WCE ranging and tracking using techniques including TOA based, PDOA based and visual motion tracking methods. We also derive the CRLB for TOA and PDOA ranging errors as the guideline of performance evaluation. The rest of this thesis is as follows: in Chapter 2, we present an overview of relevant

researches in WCE localization, including literature review in recent year and basic introduction of different kinds of localization techniques. In Chapter 3 we propose a new visual tracking algorithm for WCE localization whose performance evaluation shows its advantages over other algorithms. In Chapter 4, the CRLB of TOA ranging errors using carrier frequency is calculated and we examined the ranging errors both in homogeneous tissue and non-homogeneous tissues. Chapter 5 is composed in a quite similar way to that of Chapter 4, the PDOA using two tones signal is introduced to investigate how accurate this ranging method could be. CRLB of two tones POA based ranging errors is also calculated and compared with our results. We finally conclude our work and present the future direction of our research in Chapter 6.

Chapter 2

Overview of WCE Localization

2.1 Introduction

In this chapter we discuss the background of WCE, publications in WCE localization and some WCE localization methods. First, the basic information of WCE - the advantages and why the market demands WCE localization service - is stressed. Then we briefly investigate previous related publications in WCE localization, with different localization methods. After that, we review several fundamental localization techniques that form the basis of related publications, including TOA based , RSS based, PDOA based localization and video aided motion tracking. Analysis of advantages and disadvantages of these techniques are also posted in this chapter.

2.2 Development of Wireless Capsule Endoscope

Around twenty decades ago, Philip Bozzini made the first prototype of endoscope [13], however applying endoscopy on human body inspection was prohibited by the government until the year 1853 and it developed at an amazingly high speed from then on [14].

The birth of rod lens in the year 1960 led the shape and functions of the endoscope to becoming similar to that of today's [15], as shown in Figure 2.1.

Figure 2.1: Wired endoscope

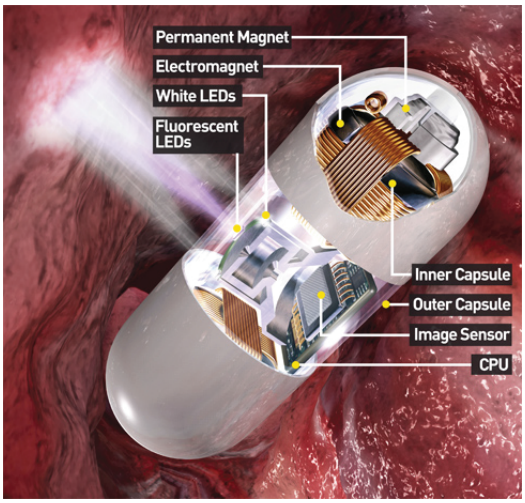

Figure 2.2: Structure of wireless endoscope

Though traditional endoscopy provides physicians with the chances to examine interior tissues of human body [16] [17], this technology causes pain and embarrassment to patients since insertion of a meter long wire could probably result in uncomfortableness [18] and invasion in human body [19] [20]. These disadvantages and our unlimited

thoughts bring out the birth of wireless capsule endoscope [21]. Wireless capsule endoscope is designed to be a pill size, swallowable and indigestible device (the overall and interior structure of WCE is shown in Figure 2.2) [22]. Since wireless capsule endoscope is equipped with one or more cameras taking photos while going through the gastrointestinal (GI) tract [23], it is also called video capsule endoscope [24].

Figure 2.3: The procedure of wireless capsule endoscopy: (a) swallow WCE, going through GI tract and transmitting images; (b) outside receivers receives images and transfers those pictures to medical workstation; (c) physicians take over the medical reviews and make decisions

First presented by Given Imaging, Yokneam, Israel in the year 2000, wireless capsule endoscope provide a noninvasive way to examine the GI tract of the human body [25]. Soon in 2001, US Food and Drug Administration cleared the electronic capsule which is designed to provide images of the GI tract [26]. The procedure of GI tract examination is given briefly here: A patient first swallow an active WCE, then the WCE start taking photos at a rate 2 frames/second during its journey in the GI tract including esophagus, stomach, small intestine and large intestine. After the entire process of digestion, the

WCE is passively expelled from human body. During its journey in the GI tract, a WCE keeps taking photos and transmitting them to outside receivers. Then, the pictures taken inside GI tract will be sent for clinical review. This procedure is shown in Figure 2.3.

However, the power consumption of camera and RF components is relatively high which makes general WCE lifetime limited to 8-12 hours [27]. Thus, WCE are gradually subdivided for more specific areas such as small intestine [28], large intestine [29]and etc. Now we can find the WCE from different companies, which are available in different types and functions. Table 2.1 shows several kinds of WCE from different companies with their properties [30] [31].

Table 2.1: Different WCE with their properties

Brand	Size (mm)	Frame rate	Battery life
Pillcam SB2	11×26	2	8 hours
Pillcam COLON	11.6×31.5	up to 35	10 hours
EndoCapsule	11×26	2	8 hours

2.3 Literature review of WCE Localization

Wireless Capsule Endoscope (WCE) is a swallowable device at the size of a pill and is equipped with one or two miniature cameras [32], going through the GI tract within typically 5-8 hours [33]. During the journey inside GI tract, it takes dozens of thousands of images with a frame rate varies from 2 to 8 frames per second which enables those frames perform as a real video. After this step, the images taken inside GI tract could then be downloaded to a mass storage device and physicians could go through the entire video and diagnose diseases in GI tract [34].

Before the birth of wireless capsule endoscopy, colonoscopy had been dominating the market for more than 50 years from the early 20th century. Though the colonoscopy is

now still the predominant way to conduct gastrointestinal (GI) tract, it is not capable to provide inspection inside small intestine. Moreover, comparing to colonoscopy, WCE provides a much more non-invasive, comfortable and non-embarrassing way to inspect patients' GI tract [35]. while taking pictures inside GI tract at a relatively high rate, WCE could record the images of abnormality and diseases and finally help doctors come up with appropriate treatment [36].

As a critical component of capsule endoscopic examination, physicians need to know the precise position of the endoscopic capsule in order to identify the position of detected intestinal abnormalities and diseases. To accurately localize the WCE, variety of localization techniques have been applied, including time of arrival (TOA) based methods, received signal strength (RSS) based methods, video based methods, video-aided hybrid localization methods,magnetic field methods and etc.

In [37], the authors discussed the possibility of RF localization of WCE, they stressed that is could be very difficult for physicians to localize the WCE using RF signals because of the complicated environment inside human body. To solve this, they designed a cyber physical system (CPS) for visualization of interior of human body to assist in their experiments. With the assistance of CPS, the challenges of WCE localization could be mainly elaborated in three aspects: modeling of WCE Movements inside GI tract, modeling of the wideband RF propagation in human body, design of algorithms for WCE localization. To meet these challenges, the authors set up a test bed and exploited a simulation software SEMCAD X to validate the their design and numerical calculation.

As one of the related project in [37], the bound of RSS localization inside human body is discussed as well as the accuracy in [38]. In this paper, simulations are conducted along with different power gradient in different organs such as stomach, small intestine and large intestine. The authors verified that 50mm average localization error is achievable in human GI tract. Meanwhile, they investigated the impact of number and topology of

sensors on localization accuracy.

Besides the RSS based localization, some papers are published on TOA based WCE localization [39] [11]. For TOA based localization of WCE, the main challenge is that human body is a mass body with dozens of organs. Thus, two directions in TOA based localization of WCE gradually arise: homogeneous tissue and heterogeneous tissue. For homogeneous tissue, it is easier for researchers to conduct experiments and simulations while less resembles real human body. For heterogeneous tissue, it is especially difficult for researchers to find the trace of signals.

Phase difference of Arrival (PDOA), however, grows to be one of the emerging localization techniques recently [40]. In the past, PDOA was considered as one of the improper localization techniques in BAN localization because of its ambiguity. But for in-body circumstances, the range between transmitter and receiver could be within several centimeters, which gives the possibility of using PDOA.

Meanwhile, video-aided localization becomes more and more popular due to the development of image processing technology. Also, the birth of cyber-physical system makes it possible to track the motion of WCE [41] [42]. In this thesis, the video-aided localization will also be discussed to investigate the accuracy of this localization technique.

2.4 Related localization techniques

2.4.1 TOA based localization

TOA based localization techniques are well-known because of their high accuracy compared to RSS based localization techniques [43]. The time of arrival is measured based on the time of travelling of RF signals between transmitter and receiver among which the location of receiver is usually unknown. TOA ranging distance could be obtained by the product of signal propagation velocity and the measured time of arrival:

$$D_{TOA} = t_{measured} * c_{\varepsilon_r} \tag{2.1}$$

where c_{ε_r} denotes the velocity of RF signals in specific medium.

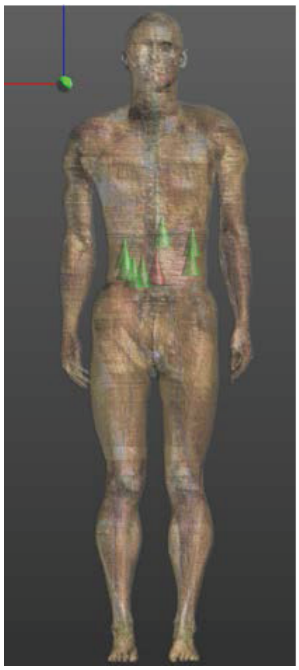

ALL TISSUES, SINGLE FREQUENCY

FREQUENCY = 402000000 Hz

Tissue name	Conductivity [S/m]	Relative permittivity	Loss tangent	Wavelength [m]	Penetration depth [m]
Air	0	1	0	0.74575	N/A
Aorta	0.56196	46.985	0.53481	0.10532	0.066888
Bladder	0.32684	19.709	0.74151	0.15855	0.076398
Blood	1.3503	64.16	0.94104	0.08547	0.034304
BloodVessel	0.56196	46.985	0.53481	0.10532	0.066888
BodyFluid	1.5296	69	0.99122	0.081819	0.031635
BoneCancellous	0.23498	22.431	0.46841	0.15351	0.10976
BoneCortical	0.091514	13.143	0.31136	0.20332	0.21278
BoneMarrow	0.029307	5.6715	0.23106	0.3111	0.43422
BrainGreyMatter	0.73833	57.396	0.57521	0.09486	0.056526
BrainWhiteMatter	0.44523	42.046	0.4735	0.11207	0.079346
BreastFat	0.034598	5.5144	0.28054	0.31455	0.36379
Cartilage	0.5871	45.448	0.57763	0.10657	0.063275
Cerebellum	1.0314	55.94	0.82445	0.093059	0.041247
CerebroSpinalFluid	2.2517	70.974	1.4186	0.075688	0.023229
Cervix	0.82274	51.603	0.71292	0.098357	0.048924
Colon	0.85873	62.557	0.61381	0.09045	0.050971
Cornea	1.1936	59.245	0.90083	0.089459	0.037078
Duodenum	1.0036	67.468	0.66517	0.086547	0.045579
Dura	0.82771	46.648	0.79342	0.10234	0.046736
EyeSclera	1.0049	57.655	0.77937	0.092233	0.042715
Fat	0.041151	5.5789	0.32982	0.31163	0.30872
GallBladder	1.1387	61.21	0.83184	0.088872	0.039121
GallBladderBile	1.6961	72.756	1.0424	0.079083	0.029516
Gland	0.87771	61.535	0.6378	0.090932	0.049604
Heart	0.96577	66.049	0.65383	0.087595	0.046798

Figure 2.4: Electrical properties for human body

However, since human body consists of heterogeneous tissues with different electrical properties such as relative permittivity and conductivity (shown in Figure 2.4) [44], the RF signal travels with different speed through different organs [45].

These variations in the speed become the main source of ranging error in ToA based localization inside the human body. Moreover, since localization resolution in and around real human bodies is usually within a range from centimeters to decimeters, highly accurate synchronization requirement is necessary which indicates an TOA error less than $1ns$. Time difference of arrival (TDOA), a closely related localization approach, could help fix this drawback. For TDOA, two or more reference nodes are allocated to measure the received signals [46]. After collecting the arrival time of received signals, time difference

is derived by doing a simple substraction. The difficulties of applying TDOA techniques are synchronization requirement and cooperation among all allocated nodes [47].

2.4.2 RSS based localization

RSS, sometimes also expressed as RSSI, is an indication of the power level being received by the antenna. When the circumstance of radio channels are known, we can build a model of the relationship between RSS and distance [48]. For RSS based WCE localization, the path-loss model plays an important role since all localization algorithms lay their foundations on the model to acquire the results. In order to improve positioning accuracy, it is necessary to develop an enough accurate in-body to surface path-loss model. In reference [49], the path-loss model in human body is given and validated, which is also shown in Table 2.2. This empirical model is supported by National Institute of Standards and Technology (NIST) and now is adopted by the IEEE group of 802.15.6 [50].

Table 2.2: Statistical parameters of implant to body surface path-loss model

Implant to body	P(d_0)/dB	α	σ/dB
deep tissue	47.14	4.26	7.85
near surface	49.81	4.22	6.81

Considering that RSS based WCE localization techniques are based on the general fact that the closer the receiver is located to the transmitter, the stronger signal the receiver receives, the relationship between the RSS and the distance between transmitter and receiver can be expressed by the path-loss model below:

$$RSS = P_t - P(d_0) - 10\alpha lg(\frac{d}{d_0}) + S(d \geqslant d_0) \tag{2.2}$$

where P_t is the transmitting power, $P(d_0)$ is the path-loss at a certain distance from transmitter, i.e., $d_0 = 50mm$, α is the power gradient from in-body tissue to body surface

and S denotes the shadow fading that performs a Gaussian distribution. Thus, from Equation 2.2, the RSS is roughly related to the distance between transmitter and receiver and the distance could be calculated if P_t is known. Figure 2.5 shows the relationship between path-loss (dB) and distance (mm) without counting in the shadow fading.

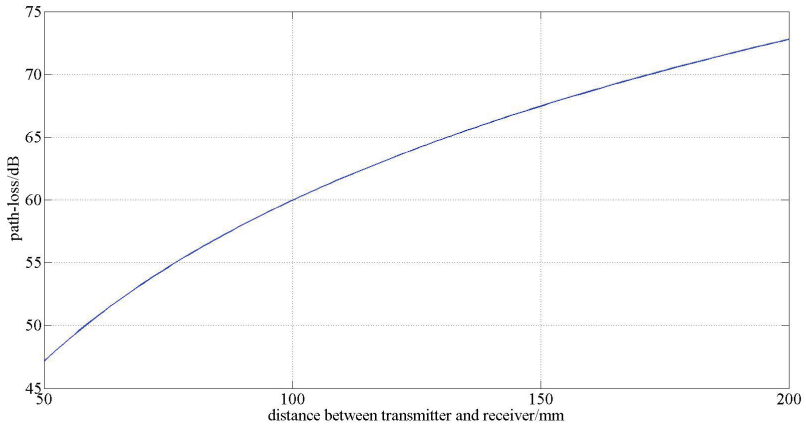

Figure 2.5: In-body to surface path-loss model

2.4.3 POA based localization

Phase of arrival gains its popularity in recent years because of the spread of Radio-frequency Identification (RFID) [51]. Now Phase Difference of Arrival (PDOA), the localization technique that develops from POA, is also considered feasible to be applied in BAN localization though POA based WCE localization is still facing some vital challenges such as phase ambiguity and phase bias when penetrating different medium. Assume that we have two RF signals at different operation frequencies f_1 and f_2, then we have

$$\phi_1 = 2\pi(\frac{df_1}{c} - n) \tag{2.3}$$

$$\phi_2 = 2\pi(\frac{df_2}{c} - n) \tag{2.4}$$

where d is the distance between transmitter and receiver, c is the speed of light in specific medium and n gives the phase ambiguity. From Equation 2.3 and 2.4, we can derive the expression of d as below:

$$d = \frac{c}{2\pi}\frac{\phi_2 - \phi_1}{f_2 - f_1} = \frac{c}{2\pi}\frac{2\pi(f_2 - f_1)\tau}{f_2 - f_1} = c \cdot \tau \tag{2.5}$$

Thus, with calculated d in Equation 2.5, we can estimate the performance of PDOA based WCE localization.

2.4.4 Video based motion tracking

Wireless capsule endoscope is usually equipped with at least one camera to provide visual inspection of the GI tract and the photos taken by the camera could be exploited not only to inspect GI tract but also to track the movement of WCE [52]. With the development of camera's capability in recent years, motion tracking using video images becomes more and more popular. To track the movement of WCE, at least two kinds of video metrics are required: displacement and rotation. Displacement distance in real world could be reflected by the scaling of view in video images and rotation angle could be estimated by measuring the rotation of view. Thus, we can tell the movement of WCE between consecutive frames by emulating the scaling and rotation angle [53].

According to Shannon's information entropy, the more similar two images are, the more mutual information they have [54]. Thus, if we iteratively change the rotation and scaling coefficients and find the maximum mutual information, we can finally acquire the displacement and rotation angle [55]. Equation 2.6 shows the way of calculating mutual information.

$$I(X,Y) = \sum_{x \in X, y \in Y} p(x,y) log(\frac{p(x,y)}{p(x)p(y)}) \tag{2.6}$$

Where X and Y are two images, $p(x)$ denotes the distribution function of gray levels at a specific pixel and $p(x,y)$ denotes the joint distribution function of gray levels.

Chapter 3

Accuracy of motion tracking of WCE inside large intestine

3.1 Introduction

During the past few years, many attempts have been made to develop accurate localization techniques for the WCE [37]. However, none of the existing localization methods is able to provide accurate position information of the endoscopic capsule due to non-homogeneous body tissues and un-uniformly distributed organs [56]. To complement the existing wireless localization infrastructures, researchers are investigating using compute vision techniques to track the motion of the video capsule [57]. Two of the most popular computer vision based motion tracking methods are scale-invariant feature transform (SIFT) [41, 58] and speeded up robust features (SURF) [59]. Both of them are usually formed in four steps: set up scale spaces, extract local features, generate descriptors utilizing surrounding pixels and map corresponding feature points [60].

Local features perform robustly when analyzing images taken inside the small intestine, at least in the upper small intestine [58]. However, things are different when WCE

goes into large intestine where local features are not as clear as those in the small intestine and the peristalsis slows down which can be observed clearly from the video taken inside large intestine. Meanwhile, with higher frame rate [61], successive images perform more globally, resembling real video rather than individual images.

In this chapter, we propose a novel approach estimating the orientation and displacement of the track of WCE in large intestine, only based on the information extracted from consecutive frames taken by WCE. This approach proceeds in four steps: (1) Apply low-pass filter on input images to smooth them, eliminating the noises and preparing for the next steps. (2) Calculate mutual information (MI) between input images [62], record the maximum MI and corresponding parameters such as orientation and scale. (3) Estimate the rotation and relative displacement of WCE according to calculated orientation and scale. (4) Performance evaluation. The main contribution of this chapter is that we introduce a more global solution to analyze the relative displacement and rotation of WCE with better performance than that of feature based applications proposed in [9, 59, 63]. Also, our approach is the measurement of WCE in large intestine while most of the related works are designed for WCE in small intestine. Moreover, this approach is much easier to be applied due to its higher linearity and stability.

The rest of this chapter is organized as follows: Section II includes details about the image analysis algorithm applied to WCE images. In section III, we talk about the experimental results and analytical comparison with other algorithms to validate the performance of our approach. Finally, in section IV, conclusion is drawn.

3.2 METHODOLOGY

Our approach basically consists of 4 steps: Pre-processing, mutual information calculation, parameter searching and performance evaluation. (a) Low-pass 2-D Butterworth

filter are implemented to eliminate the noises and guarantee the quality of the third step. (b) After the pre-processing, we calculate the mutual information of pairs of images. The more similar two images have, the more mutual information value is calculated. (c) Via searching the maximum mutual information and corresponding parameters such as scales and angles, rotation and relative displacement can be discovered so that we could tell the motion of WCE. (d) In the process of searching and performance evaluation, bicubic interpolation is frequently engaged, which can delicately help reconstruct float images.

3.2.1 Pre-processing

When the WCE passes through the large intestine, it takes images and transmits them to sensor array located outside the human body, but noises may be generated and shown in images.

Then after extraction of images from the signals sent by WCE, we transform those images into frequency domain and then apply a low-pass 2-D Butterworth filter on each frame to filter the noise (e.g. pepper or Gaussian) [64]. This step effectively guarantees the results of analysis to be robust enough. Define W as pass band and n to be order of the 2-D filter. Then the 2-D Butterworth filter can be described as

$$G^2(w) = |H(w)|^2 = \frac{1}{1 + (\frac{w}{w_c})^2 n} \tag{3.1}$$

Following Equation 3.1, 2-D IFFT is applied to transform frames back to time domain [65]. Figure 1(a) shows one of the frames with pepper noise and (b) is filtered by Butterworth filter.

Consequently, the filtered frame is obviously more smooth and is better for statistical analysis.

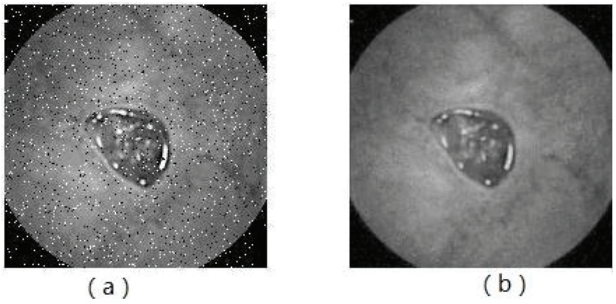

Figure 3.1: (a) Frame with salt and pepper noise (b) Frame applied Butterworth filter.

3.2.2 Mutual Information Calculation

Intuitively, the more same information two images numerically obtain, the more similar two images are. Shannons information theory lays the theoretical foundation for the hypothesis [66]. Formally, the mutual information of two images X and Y can be defined as:

$$I(X,Y) = \sum_{x \in X, y \in Y} p(x,y) log(\frac{p(x,y)}{p(x)p(y)}) \tag{3.2}$$

where p(x) and p(y) are marginal probability distribution functions of gray scales in images X and Y respectively. Eq.2 can be equivalently expressed as

$$I(X,Y) = H(X) + H(Y) - H(X \cup Y) \tag{3.3}$$

XY represents the gray scale mapping matrix of image X and Y [67]. H(X) in Equation 3.3 is the Shannon entropy of image X which can be expressed as

$$H(X) = \sum_{x \in X} p(x) log(p(x)) \tag{3.4}$$

As can be observed from Equation 3.2 to Equation 3.4, the mutual information provides a global view of similarity via statistical analysis, which is supposed to be more effective on global scale.

3.2.3 Fibonacci Searching Technique

Since the mutual information only reflects the similarity of two frames, a searching technique is required to find the maximum mutual information and the corresponding deformation. Fibonacci searching technique is a robust iterative method for searching extreme value to achieve this goal [68], performing better and is less time consuming than binary searching technique [69]. Figure 3.2 is given as the flow chart of Fibonacci searching technique.

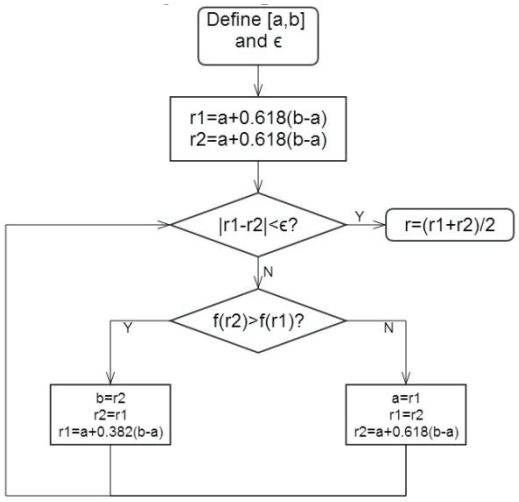

Figure 3.2: Flow chart of Fibonacci searching technique

To insure the outcomes of Fibonacci searching technique, the threshold should be small enough (e.g. 0.005). In addition, Butterworth filters smoothing effect [70] prevents the searching procedure from being stuck in a short interval with violent jitters.

3.2.4 Bicubic Interpolation

Since the float frame needs to be iteratively deformed to discover the maximum mutual information with reference frame, the new gray scales of pixels in float frame could be calculated by bicubic interpolation with higher accuracy [71]. Define f(i+u,j+v) as the

corresponding gray scale in reference frame of a pixel from float frame where $i+u$ and $j+v$ are the corresponding coordinate. Then it can be written as:

$$f(i+u, j+v) = \vec{A} * \vec{B} * \vec{C} \tag{3.5}$$

$$\vec{A} = [S(u+1) \;\; S(u) \;\; S(u-1) \;\; S(u-2)] \tag{3.6}$$

$$\vec{B} = \begin{bmatrix} f(i-1,j-1) & f(i-1,j) & f(i-1,j+1) & f(i-1,j+2) \\ f(i,j-1) & f(i,j) & f(i,j+1) & f(i,j+2) \\ f(i+1,j-1) & f(i+1,j) & f(i+1,j+1) & f(i+1,j+2) \\ f(i+2,j-1) & f(i+2,j) & f(i+2,j+1) & f(i+2,j+2) \end{bmatrix} \tag{3.7}$$

$$\vec{C} = [S(v+1) \;\; S(v) \;\; S(v-1) \;\; S(v-2)]^T \tag{3.8}$$

where S(x) is the primary function representing weights of pixels which is given by:

$$S(x) = \begin{cases} |x|^3 - 2|x|^2 + 1 & |x| < 1 \\ -|x|^3 + 5|x|^2 - 8|x| + 4 & 1 \leq |x| < 2 \\ 0 & 2 \leq |x| \end{cases} \tag{3.9}$$

Thus, the deformed frame can be reconstructed pixel by pixel smoothly.

3.3 RESULTS AND ANALYSIS

Our approach is evaluated based on 119 consecutive WCE video frames, each with 531*531 pixels resolution donated by Given Imaging.

Because of the shortage of ground truth data set to compare with, the only way is using rotation transformations and scale simulations which are also adopted by [59].

Table 3.1: Estimation of Relative Displacement

Actual scale	Calculated displacement error	Calculated displacement error in [6]	Calculated displacement error in [7]
0.2	0.0194	Large error	0.13
0.3	0.0313	13.3085	-
0.4	0.0079	0.0193	0.12
0.6	0.0031	0.0005	0.02
0.8	0.0026	0.0004	0.17
1.2	0.0011	0.0005	-
1.4	0.0013	0.0004	-
1.6	0.0016	0.0007	-
1.8	0.0097	0.0007	-
2.0	0.0009	0.0005	0.19
2.5	0.0026	0.0010	-
3.0	0.0005	0.0016	0.37

3.3.1 Orientation

Nine rotation angles from 5 to 45 with a step of 5are tested in this chapter (shown in Figure 3.3) and obtained results are shown in Table 1. This table indicates a stable performance and relatively low error throughout all the tested angles while those outcomes from [**?**,59] acquire larger errors following the increases of rotation angle.

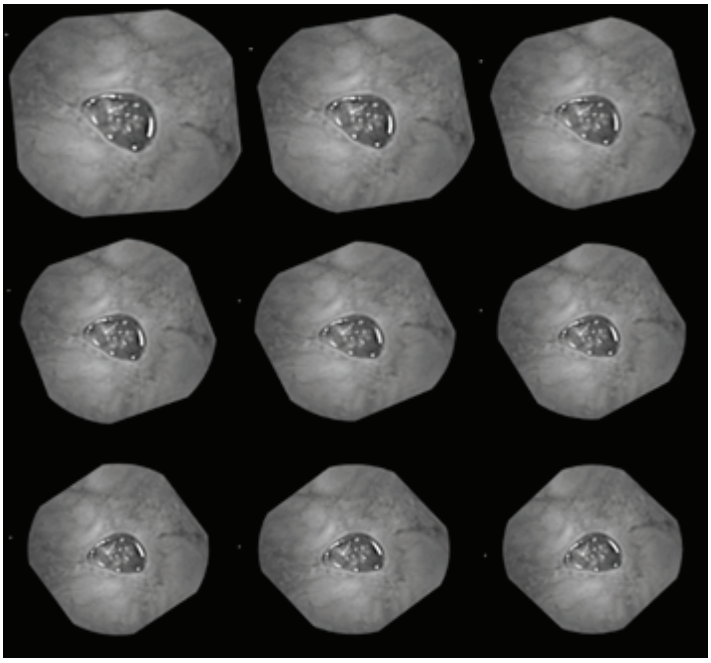

Figure 3.3: An example of tested frames, 9 rotation angles from 5 to 45 in different resolutions

Table 3.2: Estimation of Rotation

Rotation angle	Calculated orientation error (degree)	Calculated orientation error in [6] (degree)	Calculated orientation error in [7] (degree)	Calculated orientation error in [8] (degree)
5	0.0352	0.022	0.63	0.0673
10	0.0320	0.022	0.83	0.179
15	0.0453	0.026	0.90	0.403
20	0.0913	0.028	1.02	1.775
25	0.0227	0.689	0.86	0.829
30	0.0410	1.558	0.96	Large error
35	0.0844	4.719	0.92	-
40	0.0557	20.084	0.93	-
45	0.0821	30.771	0.78	-

To be more directly, we plot the statistical analysis in Figure 4 from which severe error ratios can be observed in other approaches when the rotation angle is equal or higher than 30.

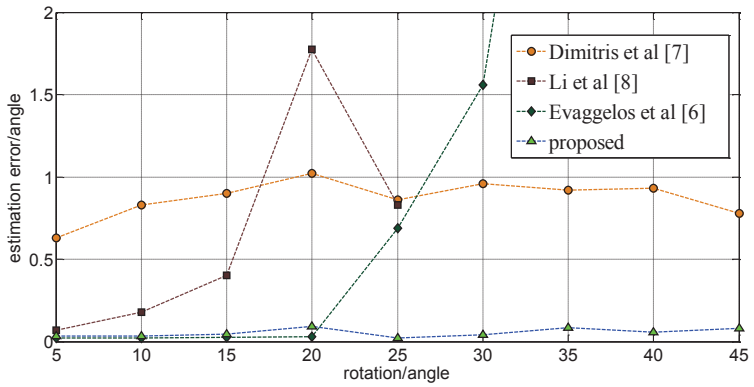

Figure 3.4: Compared experimental results of rotation estimation

3.3.2 Relative Displacement

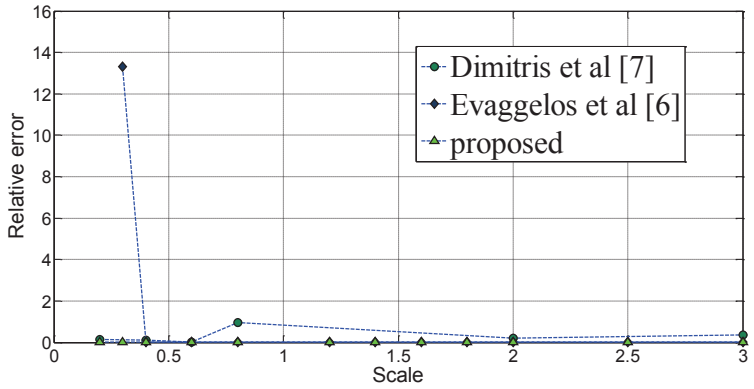

Figure 3.5: Compared experimental results of displacement estimation

In this chapter, we test 12 different scale values varying from 0.2 to 3.0, part of which is shown in Fig. 5. To transform the results from scale values to relative displacement in order to measure the motion tracking of WCE, the displacement estimation method according to projective transformation in [59] is introduced.

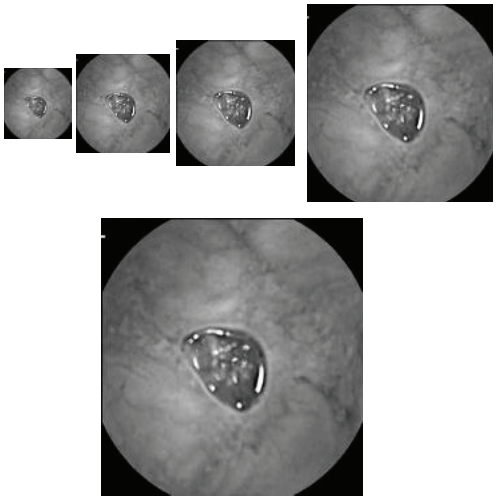

Figure 3.6: An example of frames in difference scales: 0.2, 0.3, 0.4, 0.6 and 0.8

As can be seen in Table 2, estimated displacement errors stay in the same magnitude when our approach is applied while the errors in [59] are unacceptably large when actual scale values are relatively small and decrease alone with the augment of actual scale. On the other hand, the calculated errors in [63] are about 10 times larger through the procedure of estimation. Figure 3.6 shows the overall performance quality of 3 approaches.

3.4 CONCLUSIONS

In this chapter, we proposed a novel approach to measure the motion tracking of WCE inside the large intestine. We applied maximum mutual information theory as theoretical support and Fibonacci technique as searching technique so that the measurements focus more on global information of frames. The major contribution of our research is that we utilize the global statistical information of frames rather than local features to measure the motion of WCE and achieve a higher accuracy and stability.

Chapter 4

Accuracy of TOA ranging inside human body using single tone carrier frequency

4.1 INTRODUCTION

The WCE is first swallowed by a patient, then it keeps transmitting signals from inside human body to sensors outside, as shown in Figure 4.1. Thus, the WCE could be localized by analyzing the transmitted signals and received signals. To accurately localize the WCE, variety of localization techniques have been applied, including time of arrival (TOA) based methods [72], received signal strength (RSS) based methods [38], video based methods [58], hybrid localization methods [73] and etc.

Among all these approaches for localization inside GI tract, TOA is one of the most prevalent ones. In [37] and [74], TOA based localization methods are investigated to acquire accurate localization results. Also, a number of studies have been conducted to acquire higher accuracy of in-body TOA localization. However, because of the difficulties of conducting experiments inside real body including non-homogeneous environment and inhibition of experiments inside human body, FDTD simulation is now the most efficient

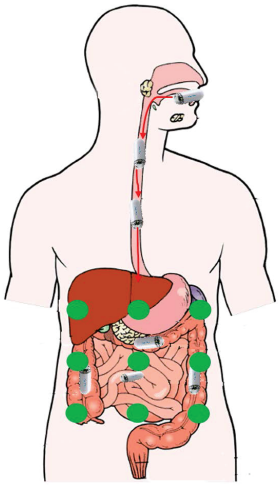

Figure 4.1: Working process of WCE

way. For instance, [10] and [11] applied TOA based localization methods to in-body localization and FDTD simulations are employed in both articles.

In this chapter we apply TOA estimation methods using 402MHz carrier frequency signals instead of wideband signals and analyze their accuracy thus there won't be ambiguity and the implementation could be much easier. With 402MHz carrier frequency within the bandwidth of BAN regulated by Federal Communication Commission (FCC) and average permittivity of 27.9 in torso part, the wavelength is $\lambda = 141.28mm$ which could cover the entire GI tract so that we can localize the WCE without any ambiguity. We also utilize the same simulation platform SEMCAD X which is also adopted in and validated by [11].

The rest of this chapter is organized as follows: In section II, the Cramer-Rao lower bound (CRLB) of TOA ranging using single tone signals inside homogeneous tissue is calculated as a guideline for the optimal performance of our approach. In section III we introduce our TOA based ranging methods and the simulation environment we accommodate. In section IV, we compare the results of TOA based ranging methods both in homogeneous and non-homogeneous tissues and analyze the source of error. Finally in

section V we draw the conclusion of this chapter.

4.2 THE CRLB OF TOA RANGING INSIDE HOMOGENEOUS TISSUE

Cramer-Rao Lower Bound, known as a lower bound for error estimation which usually indicate the limit of square of estimated errors [75],is one of the most effective ways to evaluate the performance of TOA ranging methods [76]. Define the waveform observation as:

$$r(t) = s(t-\tau) + \eta(t-\tau) \tag{4.1}$$

Then to estimate the delay τ with two sided additive Gaussian noise (AWGN) with spectral height $\frac{N_0}{2} = \sigma^2$ [77], the maximum likelihood function could be expressed as [78]:

$$f(o|\tau) = \prod_{k=1}^{K} \left\{ \frac{1}{\sqrt{2\pi}\sigma} e^{-\frac{[r_k - s_k(\tau)]^2}{2\sigma^2}} \right\} \tag{4.2}$$

where r denotes $r(t)$ and $s(\tau)$ denotes $s(t-\tau)$. Thus the likelihood function in log form is:

$$\begin{aligned} &L(o|\tau) = ln[f(o|\tau)] = \\ &ln(\prod_{k=1}^{K} \frac{1}{\sqrt{2\pi}\sigma}) + \sum_{k=1}^{K} \left\{ -\frac{1}{N_0}[r_k - s_k(\tau)]^2 \right\} \end{aligned} \tag{4.3}$$

Then by applying Eq.4 and Eq.5 we obtain the second derivative of Eq.3:

$$\frac{\partial L(o|\tau)}{\partial \tau} = \frac{2}{N_0}\sum_{k=1}^{K}\left\{[r_k - s_k(\tau)]\frac{\partial s_k(\tau)}{\partial \tau}\right\} \tag{4.4}$$

$$\frac{\partial^2 L(o|\tau)}{\partial \tau^2} = \frac{2}{N_0}\sum_{k=1}^{K}\left\{[r_k - s_k(\tau)]\frac{\partial^2 s_k(\tau)}{\partial \tau^2} - [\frac{\partial s_k(\tau)}{\partial \tau}]^2\right\} \tag{4.5}$$

Considering the fact that $\eta(t-\tau)$ is a two sided AWGN, we have $E[r_k - s_k(\tau)] = E[\eta(t-\tau)] = 0$. Meanwhile, since $\eta(t-\tau)$ is a random variable independent from both r_k and $s_k(\tau)$, $E\{[r_k - s_k(\tau)]\frac{\partial^2 s_k(\tau)}{\partial \tau^2}\} = E\{\eta(t-\tau)\frac{\partial^2 s_k(\tau)}{\partial \tau^2}\} = 0$. From the definition of waveform observation we also have $E[s_k(\tau)] = s_k(\tau)$

Therefore, the Fisher information matrix could be written as:

$$F = -E[\frac{\partial^2 L(o|\tau)}{\partial \tau^2}] = -\frac{2}{N_0}\sum_{k=1}^{K}\left\{-[\frac{\partial s_k(\tau)}{\partial \tau}]^2\right\} \tag{4.6}$$

Letting $K \to \infty$, Eq.6 turns from discrete version into continuous version:

$$F = -E[\frac{\partial^2 L(o|\tau)}{\partial \tau^2}] = \frac{2}{N_0}\int_{T_0}[\frac{\partial s(\tau)}{\partial \tau}]^2 \tag{4.7}$$

where T_0 is the observation time.

To acquire a more specific CRLB of TOA using sinusoidal carrier frequency signal with limited observation time, we define

$$s(\tau) = s(t-\tau) = Acos[w_c(t-\tau)] \tag{4.8}$$

Then to obtain the same result in Eq.7, we must calculate the square of first derivative of $s(\tau)$:

$$\frac{\partial s(\tau)}{\partial \tau} = Aw_c sin[w_c(t-\tau)] \tag{4.9}$$

$$
\begin{aligned}
[\frac{\partial s(\tau)}{\partial \tau}]^2 &= A^2 w_c^2 sin^2[w_c(t-\tau)] \\
&= \frac{1}{2}A^2 w_c^2\{1-cos[2w_c(t-\tau)]\}
\end{aligned}
\tag{4.10}
$$

Define $I_\tau(t,\tau)|_0^{T_0} = \int_{T_0}[\frac{\partial s(\tau)}{\partial \tau}]^2 dt$, $I_s(t)|_0^{T_0} = \int_{T_0}[s(t)]^2 dt$ then we have:

$$
I_\tau(t,\tau)|_0^{T_0} = \{\frac{1}{2}A^2 w_c^2 t - \frac{1}{4}A^2 w_c sin[2w_c(t-\tau)]\}|_0^{T_0} \tag{4.11}
$$

$$
I_s(t)|_0^{T_0} = \frac{A^2 sin2tw_c + 2tw_c}{4w_c}|_0^{T_0} = E_s \tag{4.12}
$$

where E_s is the energy of time-limited single tone signal.

Meantime, with fixed SNR, we could derive the expression of N_0. In [79], the SNR is written as:

$$
SNR = \frac{P_s}{P_n} = \frac{E_s/T_0}{N_0 W} \tag{4.13}
$$

where W represents the system bandwidth.

Thus N_0 could be presented as:

$$
N_0 = \frac{P_s}{P_n} = \frac{E_s/T_0}{SNR \cdot W} \tag{4.14}
$$

Taking Eq.7-14 as a whole, we consequently come to the final expression of Fisher information matrix:

$$F = -E[\frac{\partial^2 L(o|\tau)}{\partial \tau^2}] = \frac{2}{N_0}\int_{T_0}[\frac{\partial s(\tau)}{\partial \tau}]^2 \\ = \frac{2SNR \cdot WT_0 I_\tau(t,\tau)|_0^{T_0}}{I_s(t)|_0^{T_0}} \tag{4.15}$$

The CRLB of TOA using carrier frequency is shown in Eq.16, which is the inverse of the Fisher information matrix [78] in Eq.15:

$$\sigma_\tau^2 = F^{-1} = \frac{I_s(t)|_0^{T_0}}{2SNR \cdot WT_0 I_\tau(t,\tau)|_0^{T_0}} \tag{4.16}$$

Taking homogeneous tissue with permittivity ε_r and speed of light C into consideration, the bound for TOA ranging error should be:

$$\sigma_d = \frac{c}{\sqrt{\varepsilon_r}} F^{-1} \tag{4.17}$$

4.3 SIMULATION ENVIRONMENT AND METHODOLOGY FOR TOA BASED RANGING

4.3.1 Simulation Environment

To examine the performance of our TOA based methods, the simulations are carried out by SEMCAD X, a finite difference time domain (FDTD) based simulation platform provided by SPEAG, Swiss. SEMCAD X performs faster FDTD simulations when comparing with other simulation software while it still holds high accuracy [80].

Figure 4.2 shows the realistic cyber phantom provided by SEMCAD X with seventy seven organs. This phantom is originally designed to emulate the electromagnetic environment of human body thus it could be used to simulate the propagation of RF signals

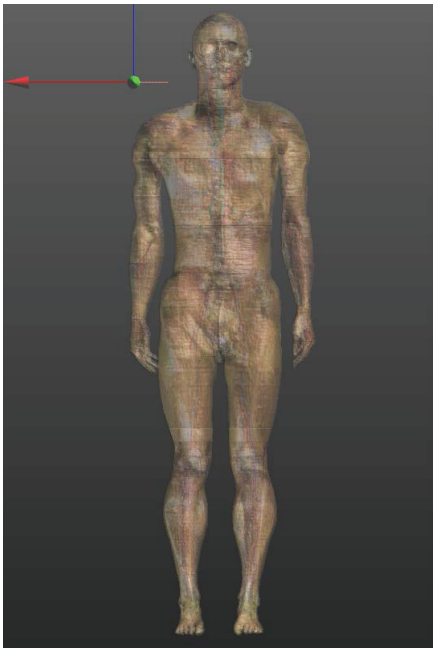

Figure 4.2: Phantom for simulation

inside and outside human body. In our simulations, Dielectric properties of tissues are configured for 402MHz frequency, within the interval of 402-405MHz which is allocated by FCC.

4.3.2 Methodology

Detection of First Peak

Detection of the first peak is a simple and intuitional but the most frequently used TOA ranging method in BAN, especially when using UWB signals.

Define the transmitted signal as $s(t)$ and the received signal as $r(t) = s(t-\tau) + \eta(t-\tau)$

Then the time delay for detection of first peak is estimated by:

$$\tau = |arg\ min\{T_{arg\ max\ s(t)}\} - arg\ min\{T_{arg\ max\ r(t)}\}| \tag{4.18}$$

Detection of All Peaks

Though the detection of first peak is widely used in TOA based localization in BAN, its accuracy is somehow greatly affected by the noise. To weaken the impact of noise, we could exploit the fact that the transmitted carrier frequency signals are sinusoidal signals, i.e., periodic signals. The number of peaks will be more than one if the observation time is long enough.

We first acquire all the peaks in transmitted signal:

$$\mathbf{T_s} = [s_1, s_2, ..., s_n]^T \tag{4.19}$$

Considering that the received signal is noised, we could segment the received signal into pieces with length of one period, obtain the peaks in every piece and then form a vector of detected peaks in received signal:

$$\mathbf{T_r} = [r_1, r_2, ..., r_n]^T \tag{4.20}$$

Thus the estimated TOA is:

$$\tau = \frac{\sqrt{\mathbf{T}_\tau{}^T} \cdot \sqrt{\mathbf{T}_\tau}}{n} \tag{4.21}$$

where $\mathbf{T}_\tau = \mathbf{T_r} - \mathbf{T_s}$

Generalized Correlation Coefficients

Generalized Cross Correlation (GCC) is an estimation methods for time delay which was usually applied in radar system instead of UWB system [81]. Since our simulation are conducted with carrier frequency 402 MHz, it matches quite well with this GCC methods. Define received signal as $r(t) = s(t-\tau) + \eta(t-\tau)$, then we have the cross-correlation

between transmitted and received signals to be

$$R(\tau) = E[r(t)s(t)] = E[s(t)s(t-\tau) + s(t)\eta(t-\tau)] \tag{4.22}$$

Since $\eta(t-\tau)$ is an additive white Gaussian noise which is independent from $s(t)$,

$$E[s(t)\eta(t-\tau)] = 0 \tag{4.23}$$

$$R(\tau) = E[s(t)s(t-\tau)] \tag{4.24}$$

Thus, according to the definition of autocorrelation function, we can observe that the maximum value of $R(\tau)$ at the time $t = \tau$

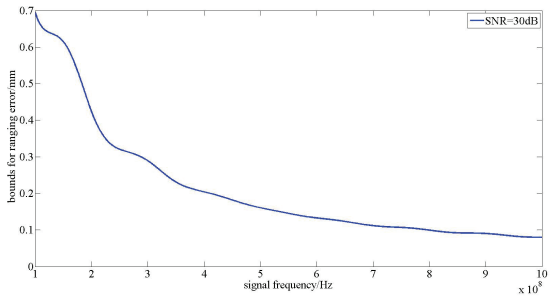

Figure 4.3: Relationship between signal frequency and TOA ranging error inside homogeneous tissue

4.4 RESULTS AND ANALYSIS

4.4.1 Bounds for TOA ranging error

As can be seen from the derivation of CRLB in Section II, the bound of TOA ranging inside homogeneous tissue is related to a couple of physical coefficients, including W, SNR, w ,T_0 andε_r.

In this subsection, we will mainly discuss the effects of w while the coefficients W ,SNR, ε_r and T_0 that related to capability and configuration of simulation system or related to the environment are fixed as: $W = 10GHz, T_0 = 25ns$, $SNR = 30dB$, $\varepsilon_r = 27.9$, among which the value of ε_r is calculated in [11] as the average permittivity of human body around torso part.

The relationship between signal frequency and TOA ranging error inside homogeneous tissue is shown in Figure 4.3. From this figure we can easily observe the fact that the bound of TOA ranging error inside homogeneous tissue drops alone with the increase of signal frequency, i.e., they are negatively correlated.

4.4.2 Accuracy of Different TOA Ranging Methods inside Homogeneous Tissue

To investigate the accuracy of TOA ranging methods interpreted in Section III, we allocated the WCE at 4 different positions inside GI tract of the phantom for simulation. The distances between WCE and skin-mounted sensor range from 75.948mm to 134.231mm. And to find the source of error, we didn't add any noise to simulations. Table 1 shows the TOA ranging error without noise. Since there is no noise added, these errors are supposed to be systematic error and quantization error.

Table 4.1: ranging error without noise unit: mm

Distance	Detection of First Peak	Detection of All Peaks	GCC
75.948	0.09	0.08	0.08
98.951	0.085	0.083	0.083
120.637	0.087	0.088	0.085
134.231	0.104	0.101	0.101

After the simulation without noise, we conducted the simulations with $SNR = 30dB$ to emulate the accuracy of different TOA ranging methods. Figure 4.4 shows the ranging er-

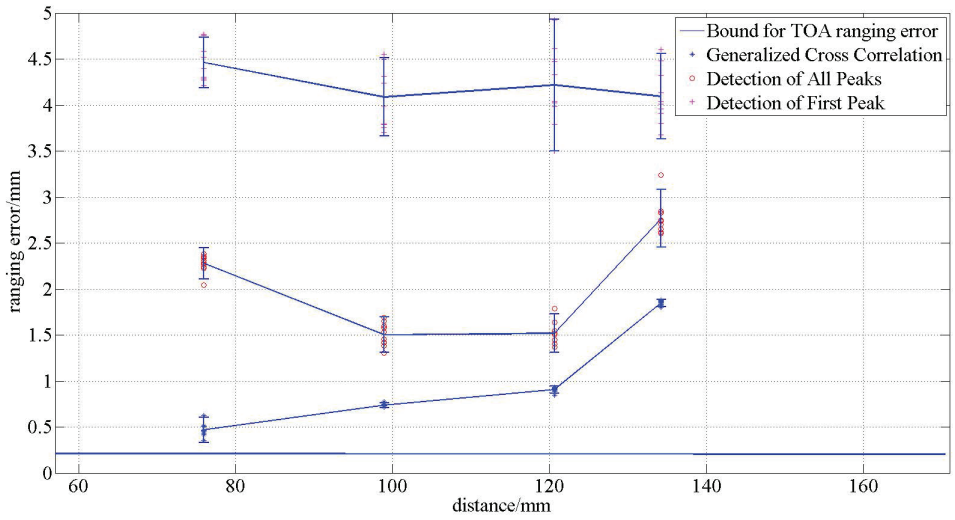

Figure 4.4: Relationship between signal frequency and TOA ranging error inside homogeneous tissue

rors of three TOA ranging methods inside homogeneous tissue. In spite of the systematic error and quantization error shown in Table 1, it is obvious that GCC performs a highest accuracy among these methods and stays closer to the bound while detection of the first peak reveals the largest error as well as deviation.

This observation can be explained if we review the characteristics of the TOA ranging methods in Section III. Since detection of the first peak only make the use of first peak, the AWGN has the most severe impact on its accuracy. While detection of all peaks exploit all the detected peaks during the observation time, the algorithm of GCC involves all points of signals, which indicates the best resistance to AWGN.

4.4.3 Accuracy of Different TOA Ranging Methods inside Non-homogeneous Tissue

We analysis the accuracy of TOA ranging methods inside homogeneous in last subsection. In practical environment, however, tissues of human body are usually non-homogeneous.

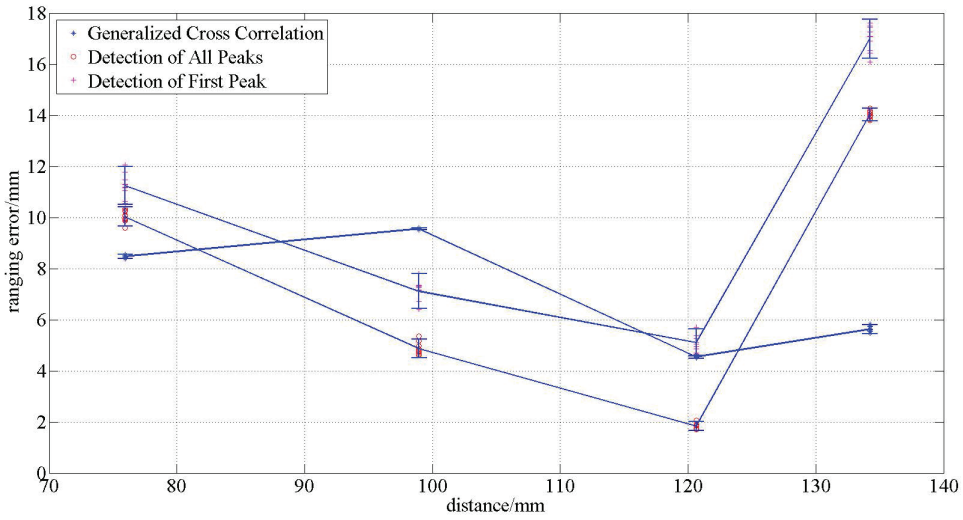

Figure 4.5: Relationship between signal frequency and TOA ranging error inside non-homogeneous tissue

Thus, we import the dielectric properties of body tissues at 402MHz into our simulation to estimate the impact of non-homogeneity on the accuracy of TOA ranging methods.

Figure 4.5 shows the ranging error versus distance inside non-homogeneous tissues. Different from what we have observed from Figure 4.4, the ranging error of GCC doesn't show apparent advantages of its accuracy. On the other hand, GCC still keeps its better stability over the other ranging methods. Moreover, TOA ranging errors inside non-homogeneous increase enormously when comparing to that inside homogeneous tissue. For instance, the maximum errors of GCC, detection of all peaks and detection of the first peak are about 1.85*mm*, 3.30*mm* and 5.02*mm* in homogeneous tissue, respectively; Whereas their maximum errors rise to around 9.5*mm*, 14.2*mm* and 17.7*mm*.

Comparing the statistics from Table 1 and those from Figure 4.4 and 4.5, it is obvious that the systematic errors and quantization errors are trivial. Meanwhile, considering that the only difference between simulations with homogeneous tissue and simulations with non-homogeneous tissue is the change of dielectric properties, we can draw the conclusion that the non-homogeneity is one of the major sources of ranging error in non-

homogeneous tissues.

4.5 Conclusion

In this chapter, we proposed the CRLB of TOA ranging inside homogeneous tissue using carrier frequency signals and analyzed the accuracy of three TOA ranging methods inside GI tract. Among previous TOA ranging methods using carrier signals, neither detection of all peaks nor GCC has been applied to localization approaches inside GI tract. We also conducted simulations both with homogeneous tissue and non-homogeneous tissues to investigate the performance of our TOA ranging methods. Meanwhile, we analyzed the influence of non-homogeneity on ranging accuracy. Our future research will be concentrated in the same area but focus more on non-homogeneous tissue which resembles realistic human body, designing and applying new algorithms to improve the accuracy of in-body TOA ranging and localization techniques.

Chapter 5

Accuracy of PDOA ranging inside human body using two tones

5.1 Introduction

There are some requirements for localization information in BAN applications, for example, positioning the wearable and implant sensors, in order to help the doctor to decide where the needed target is. WCE, for example, needs the location information. The capsule transmits the RF signal from inside human body to the sensor in the surface of the human body or to another sensor inside human body [82] [11]. Several approaches have been developed by researchers to estimate the capsule location. Two traditional technologies of RF localization are based on Time of Arrival (TOA) and Received Signal Strength (RSS) [45].

In reference [37], the authors claims that the next step in the evolution of RF localization science is the transformation into RF localization inside the human body. The first major application for this technology is the localization of the wireless video capsule endoscope (VCE). In the paper, authors described how they can design a cyber-physical

system (CPS) for experimental testing and visualization of interior of the human body that can be used for solving the RF localization problem for the endoscopy capsule. The authors also addressed the scientific challenges and the appropriate technical approaches for solving the problem.

In reference [83], authors studied how to estimate the exact position of the capsule. In the paper, the authors proposed a novel localization method based on spatial sparsity, and directly estimated the location of the capsule without going through the usual intermediate stage of first estimating time-of-arrival or received-signal strength, and then a second stage of estimating the location. The results show that the proposed method is effective and accurate, even in massive multipath conditions.

In order to get a better accuracy of localization in BAN application, people also need to study the channel model in and out of the body [84] [85] [86] [87]. Some papers have studied in-body path loss model for homogeneous human tissues and achieved some good results [88] [89]. In reference [90], voltage and power transfer functions for the path loss of a 402 MHz body-area network are also reviewed. It was shown that basic FDTD simulations for a homogeneous human-body model, implemented in MATLAB, agreed quite well with the advanced FEM solver for an inhomogeneous accurate human-body model. The frequency bands used in BAN are focused on 402MHz and 2.4GHz. For these two frequency bands, TOA and RSSI based ranging have some shortcomings. As is know, TOA based ranging method usually needs wider bandwidth, and RSS based ranging has low accuracy of position [79]. Further more, TOA based ranging method using narrow band signal has a problem of ambiguity.

Although there are many papers describing BAN based ranging and positioning, one subject is not discussed until now. That is using PDOA based ranging behaviors for BAN applications. In this chapter we analyze phase difference of arrival (PDOA) based ranging in BAN application. This chapter is organized as follows. In section II, we analyze the

PDOA based ranging principle and characteristics. In section III, we analyze the cramer-rao lower bound (CRLB) for PDOA ranging method. In section IV, we use ray tracing method to model the distance and bandwidth influence on PDOA based ranging in BAN. In section V we use simulation software to study the PDOA based ranging. In section VI, we do some measurements to testify the PDOA method. These includes the measurement setup and scenario, including the equipment and antennas used in the measurement.

5.2 POA based ranging principle and characterization

5.2.1 Phase of single tone

As we all know, three parameters representing a sine wave are amplitude, frequency and phase [91]. Phase of arrival must be a valid method for ranging. But few people have focused their researches on phase parameter. Actually, in some circumstances, PDOA based ranging is similar with TDOA based ranging method. Supposed the distance between source and sensor in a homogenous tissue is d, if the electromagnetic transmission velocity in vacuums is c, the relative average permittivity for a certain area of body is ε_r, v is the electromagnetic transmission velocity in a homogenous tissue, λ is its wavelength, we can easily get the time of arrival at the sensor:

$$\tau = \frac{d}{v} = \frac{d \cdot \sqrt{\varepsilon_r}}{c} = \frac{d}{f\lambda} \tag{5.1}$$

The phase of arrival ϕ satisfies the equation

$$\phi + 2\pi n = 2\pi f \tau \tag{5.2}$$

where n is the passed number of whole cycles. If using single tone for POA based ranging, in order to avoid the phase ambiguity, we must adopt a not very high frequency

to get a comparatively bigger wavelength.

In multipath environments, Fig. 5.1 shows how multipath components add up together. A_i is the amplitude of each path and ϕ_i is the phase of each path.

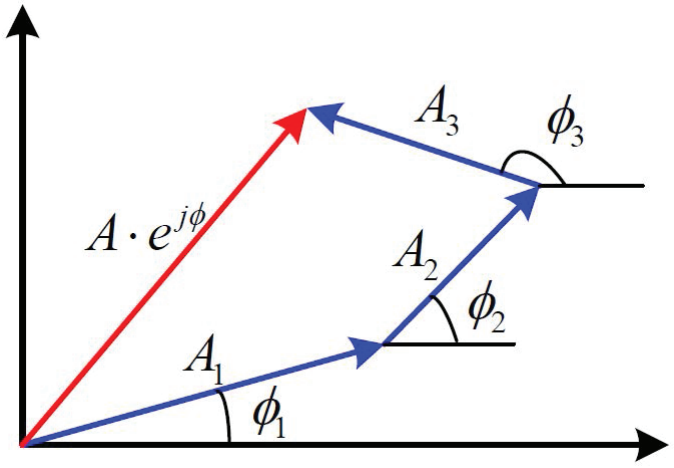

Figure 5.1: signal phases in multipath environment

5.2.2 Phase difference of Two tones

Since the range of the phase measurement is between 0 and 2π, it would be necessary to recognize the passed number of whole cycles n in order to determine the distance greater than λ. The ambiguity can be eliminated by sending two tones and measuring the difference between their received delay phases. We get:

$$\phi_1 = 2\pi(\frac{df_1}{v} - n) \tag{5.3}$$

$$\phi_2 = 2\pi(\frac{df_2}{v} - n) \tag{5.4}$$

Subtract Equation 5.3 from 5.4 then we have

$$d = \frac{v}{2\pi}\frac{\phi_2 - \phi_1}{f_2 - f_1} = \frac{v}{2\pi}\frac{2\pi(f_2 - f_1)\tau}{f_2 - f_1} = v \cdot \tau \tag{5.5}$$

The ambiguity in range is eliminated. The span of the measurement of ϕ is 2π, and the maximum value of d that can be measured using phase difference of two tones is conditioned on a maximum two tones frequency bandwidth.

For example, if the average electromagnetic velocity in the human body is $0.568e8m/s$, interval between $f2$ and $f1$ is 20MHz, the maximum measurable one-way distance is $2.84m$. Let $\delta\phi$equals a given phase difference measurement error, then the distance error δd could be written as:

$$\delta d = \frac{v}{2\pi}\frac{\delta\phi}{\Delta f} \tag{5.6}$$

where $\Delta f = f_2 - f_1$. It is clear from equation 5.6 that the error increases in inverse proportion to the frequency difference. As Δf is made smaller to accommodate longer range, the resolution or ranging error increases.

5.3 CRLB of PDOA ranging in AWGN channel

We use two tones $f1$ and $f2$ to calculate the CRLB for PDOA based ranging, and suppose each tone has the power of $W * S0/4$, which is shown in Figure 5.2.

Two tones spectrum consists of two impulses. The transmitted pulse is $s(t)$, and the observed signal at the receiver is given by:

$$r(t) = s(t - \tau) + \eta(t - \tau) \tag{5.7}$$

Then to estimate the delay τ with two sided additive Gaussian noise (AWGN) with spectral height $\frac{N_0}{2} = \sigma^2$, the maximum likelihood function could be expressed as [78]:

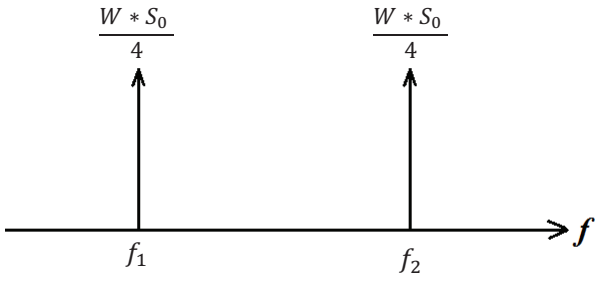

Figure 5.2: signal phases in multipath environment

$$f(o|\tau) = \prod_{k=1}^{K} \left\{ \frac{1}{\sqrt{2\pi}\sigma} e^{-\frac{[r_k - s_k(\tau)]^2}{2\sigma^2}} \right\} \tag{5.8}$$

where r denotes $r(t)$ and $s(\tau)$ denotes $s(t-\tau)$. Thus the likelihood function in log form is:

$$\begin{aligned} &L(o|\tau) = ln[f(o|\tau)] = \\ &ln(\prod_{k=1}^{K} \frac{1}{\sqrt{2\pi}\sigma}) + \sum_{k=1}^{K} \left\{ -\frac{1}{N_0}[r_k - s_k(\tau)]^2 \right\} \end{aligned} \tag{5.9}$$

Then by applying Eq.4 and Eq.5 we obtain the second derivative of Eq.3:

$$\frac{\partial L(o|\tau)}{\partial \tau} = \frac{2}{N_0} \sum_{k=1}^{K} \left\{ [r_k - s_k(\tau)] \frac{\partial s_k(\tau)}{\partial \tau} \right\} \tag{5.10}$$

$$\frac{\partial^2 L(o|\tau)}{\partial \tau^2} = \frac{2}{N_0} \sum_{k=1}^{K} \left\{ [r_k - s_k(\tau)] \frac{\partial^2 s_k(\tau)}{\partial \tau^2} - [\frac{\partial s_k(\tau)}{\partial \tau}]^2 \right\} \tag{5.11}$$

Considering the fact that $\eta(t-\tau)$ is a two sided AWGN, we have $E[r_k - s_k(\tau)] = E[\eta(t-\tau)] = 0$. Meanwhile, since $\eta(t-\tau)$ is a random variable independent from both r_k and $s_k(\tau)$, $E\{[r_k - s_k(\tau)]\frac{\partial^2 s_k(\tau)}{\partial \tau^2}\} = E\{\eta(t-\tau)\frac{\partial^2 s_k(\tau)}{\partial \tau^2}\} = 0$. From the definition of waveform observation we also have $E[s_k(\tau)] = s_k(\tau)$

Therefore, the Fisher information matrix could be written as:

$$F = -E[\frac{\partial^2 L(o|\tau)}{\partial \tau^2}] = -\frac{2}{N_0}\sum_{k=1}^{K}\left\{-[\frac{\partial s_k(\tau)}{\partial \tau}]^2\right\} \tag{5.12}$$

Letting $K \to \infty$, Eq.6 turns from discrete version into continuous version:

$$F = -E[\frac{\partial^2 L(o|\tau)}{\partial \tau^2}] = \frac{2}{N_0}\int_{T_0}[\frac{\partial s(\tau)}{\partial \tau}]^2 \tag{5.13}$$

where T_0 is the observation time.

Plug Equation 5.13 into Parseval's theorem, we have

$$F = \frac{1}{\pi N_0}\int_{-\infty}^{\infty}\omega^2|S(\omega)|^2 d\omega \tag{5.14}$$

Therefore the CRLB representing the variance of estimation is given by

$$\begin{aligned} CRLB = F^{-1} &= \frac{\pi N_0}{\int_{-\infty}^{\infty}\omega^2|S(\omega)|^2 d\omega} = \\ &\frac{\pi N_0}{\int_{f_0-W/2}^{f_0+W/2}(2\pi f)^2\frac{S_0}{4}W[\delta(f-f_0+\frac{W}{2})+\delta(f-f_0-\frac{W}{2})]2\pi df} = \\ &\frac{1}{8\pi^2(f_0^2+\frac{W^2}{4})SNR\cdot T_0} \end{aligned} \tag{5.15}$$

Thus, the CRLB of ranging error using two tones PDOA based ranging is

$$\sigma_d \geqslant v\cdot\sqrt{\frac{1}{8\pi^2(f_0^2+\frac{W^2}{4})SNR\cdot T_0}} \tag{5.16}$$

Compared with CRLB of RSSI $\frac{\sigma ln10}{10\alpha}$, we can get the comparison results. σ is the variance of AWGN, α is the power gradient, d is the distance. Suppose $\sigma = \sqrt{5}$, $\alpha = 3$, $d = 0.1m$, the CRLB of RSSI is $0.017m$. Compare this result with Figure 5.3 and 5.4, we can conclude PDOA based ranging is more accurate than RSSI based ranging.

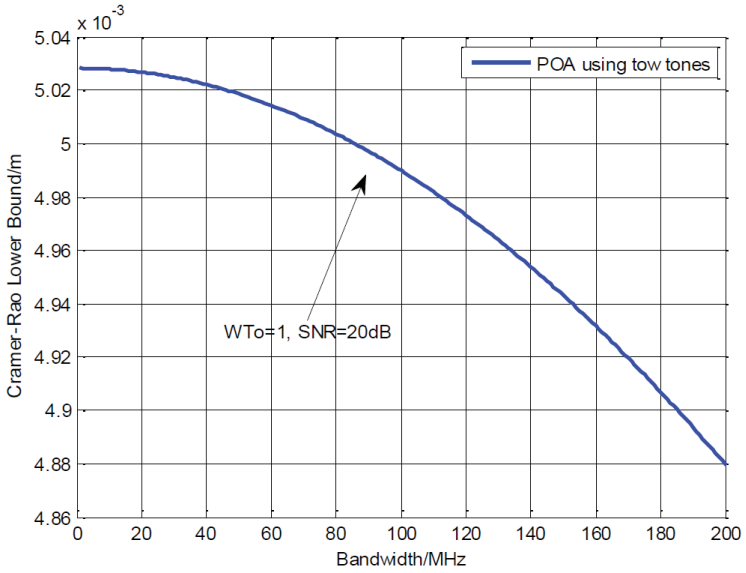

Figure 5.3: CRLB of PDOA based ranging ($WT_0 = 1$)

Supposed $WT_0 = 1$, we can obtain the simulation result. Figure 5.3 demonstrates the CRLBs of PDOA with two tones based ranging. As the bandwidth increases, the PDOA based ranging with two tones becomes more accurate. T_0 is the waveform interval which represents the signal waveform duration cycle. Supposed T0=1/1M, we can obtain another simulation result. Figure 5.4 demonstrates the CRLBs of PDOA with two tones based ranging. As the bandwidth increases, the PDOA based ranging with two tones is more accurate than RSSI based ranging.

So we may draw a conclusion that two tones PDOA based ranging could be more accurate for ranging.

5.4 PDOA based ranging with ray tracing in multipath environment

Ray tracing is a good way to evaluate the performance of multipath impact on localization when the circumstance is relatively uncomplicated [92]. In order to characterize the

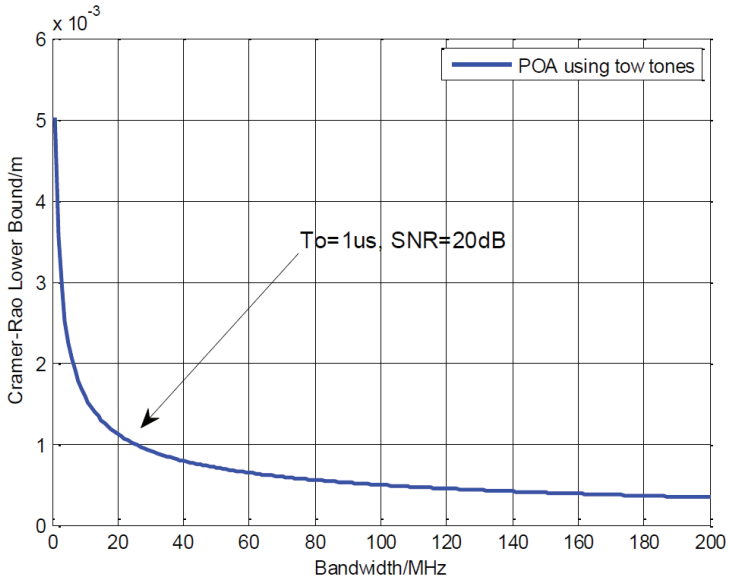

Figure 5.4: CRLB of PDOA based ranging ($T_0 = 1us$)

method of PDOA based ranging, we use ray tracing method to study the ranging performance in one scenario in Figure 5.5. In this simulation, we define that there are three paths in the time channel profile. Figure 5.6 is the time delay profile results of ray tracing simulation.

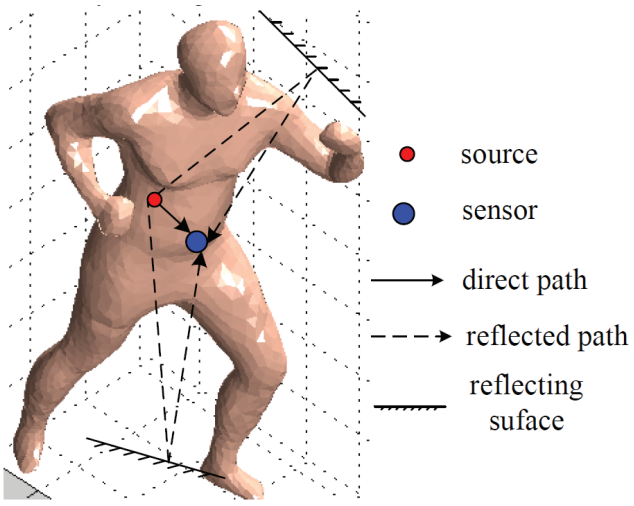

Figure 5.5: The simulation scenario for ranging a tag with Ray Tracing

According to reference, the authors calculate the average permittivity of the human

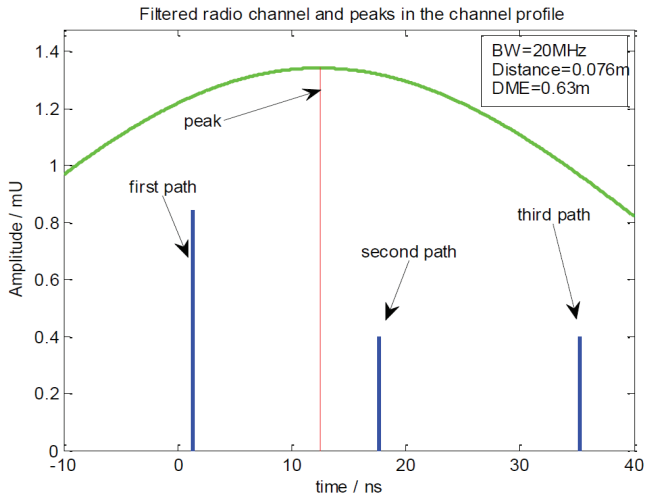

Figure 5.6: Channel time profile with 3 paths

body as $\varepsilon_r = 27.9.$, and compute the average velocity in the human body as $v = 0.568 \times 10^8 m/s$. When 20MHz bandwidth is applied, from Figure 5.6 and Table 5.1, we can see the TOA base ranging distance error is 0.629 which is much bigger than actual distance value. Compared with Table 5.2, the POA based ranging distance error is much smaller than that of TOA based ranging. Figure 5.7 shows the distance error using ray tracing versus the calculated CRLB. In Figure 5.8, the results of distance measurement using PDOA in different frequency bands are shown.

In order to explain the ranging behavior of PDOA methods more clearly, we draw the Table 5.2. Table 5.2 shows PDOA based ranging parameters in comparison of different frequency bands with Ray Tracing in multipath environment.

Table 5.1: Results of ray tracing in multipath environment

Bandwidth	First TOA	Real Distance	Measured Distance	Measured Distance
20MHz	1.338ns	0.076m	0.7056m	0.62959m

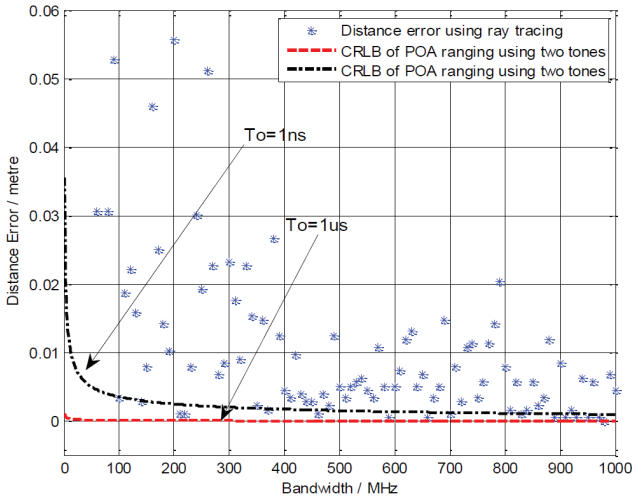

Figure 5.7: Distance error using ray tracing versus the CRLB

Table 5.2: PDOA based ranging with Ray Tracing in multipath environment (real distance is 0.076m)

Bandwidth/MHz	Number of points	Measured mean	Measured variance	Distance error
400-420	21	0.081m	1.3e-4	0.005m
2440-2460	21	0.0646m	4.2e-5	0.0114m

5.5 PDOA based ranging with simulation in SEMCAD X

To validate the performance of our PDOA based methods, we conduct simulations in SEMCAD X, a finite difference time domain (FDTD) based simulation platform which is proved to be faster than other simulation software. Figure 5.9 is the photograph of experiment of ranging a source in the body. Figure 5.10 shows distance measurement results.

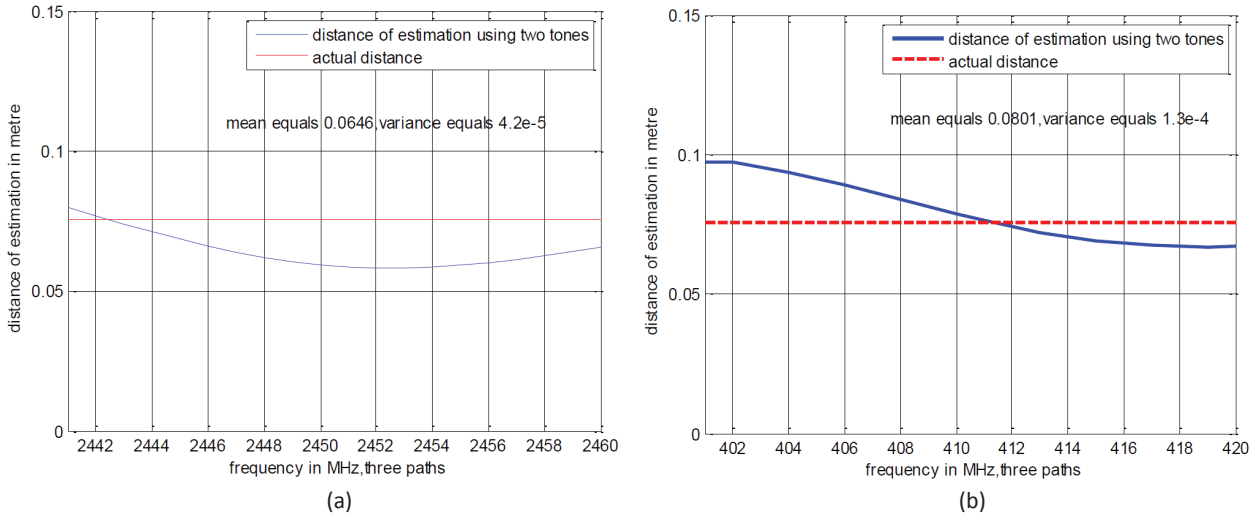

Figure 5.8: (a) distance measurement using PDOA around 2.45GHz; (b) distance measurement using PDOA around 402MHz

5.6 PDOA based ranging with measurement in physical phantom environment

We also have conducted some measurements for research of POA based ranging in anechoic chamber space. We use Agilent network analyzer E8363B and a pair of BAN antennas to simulate the ranging scenario, as is shown in Figure 5.11. Table 5.3 shows some measurement results in anechoic chamber environment.

5.7 conclusion

In this chapter we address the ranging problem for BAN application which are useful for future medical wearable and implanted electronic devices. Different from those common

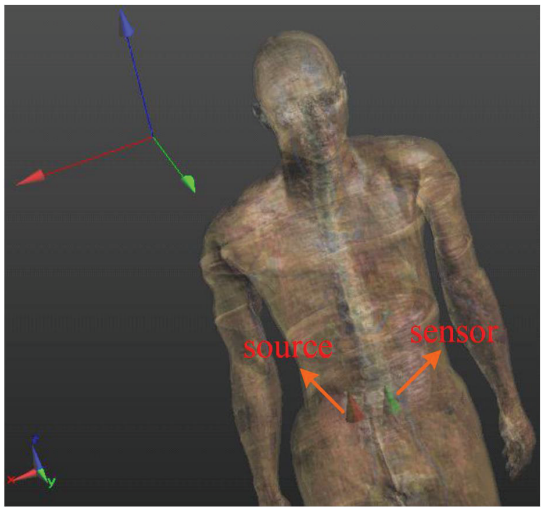

Figure 5.9: PDOA ranging scenario for in-body BAN using SEMCAD X

Table 5.3: POA based ranging with Ray Tracing in multipath environment (real distance is 0.076m)

Actual distance	Bandwidth/MHz	Measured distance/m	Distance error/m
0.15	400-420	0.181	0.031
0.15	2440-2460	0.178	0.028
0.25	400-420	0.279	0.029
0.25	2440-2460	0.275	0.025

methods such as RSS and TOA techniques, we propose phase difference of arrival based method for ranging in BAN and study its channel characteristics. First, we analyze the PDOA based ranging principle and characteristics. Second, we analyze the cramer-rao lower bound (CRLB) for PDOA ranging method. Third, we use ray tracing method to model the distance and bandwidth influence on PDOA based ranging in BAN. Fourth, we use simulation software SEMCAD to study the POA based ranging. Fifth, we do some measurements n anechoic chamber to test the POA method. The research results show that in BAN application, POA based ranging has a good performance. It will benefit the future reference use of choosing PDOA ranging method for BAN application.

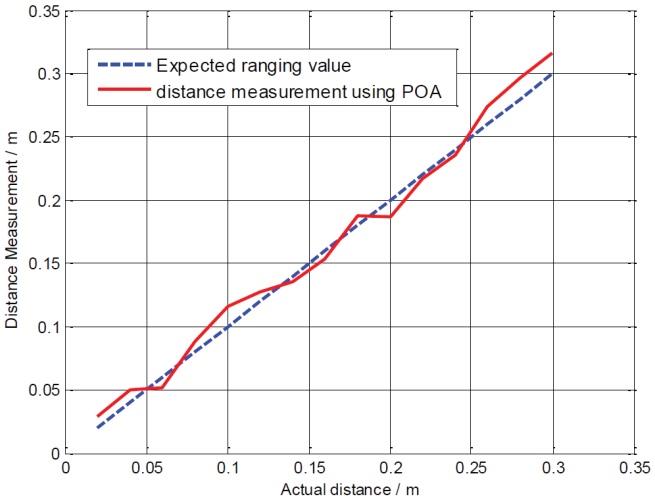

Figure 5.10: Expected and simulated distance in homogenous tissue

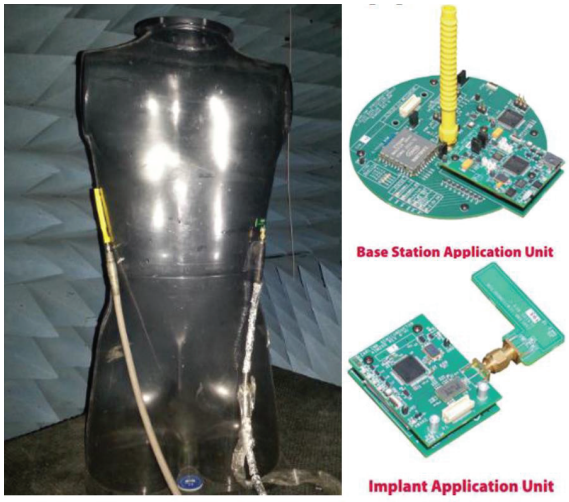

Figure 5.11: Measurement scenario—Dual band antenna (402 MHz + 2.45 GHz) for operation in BAN

Chapter 6

Conclusion and Future Directions

This chapter presents an overall conclusion of the thesis and provides some possible future directions of researches in this area.

6.1 Conclusion

In this thesis, investigation of the accuracy of WCE localization have been done. The work consists of three parts: video motion tracking of WCE in large intestine, TOA based ranging inside human body, and PDOA based ranging inside human body. All these different parts of our work focus on the accuracy of WCE localization. And the conclusion of our work is drawn and listed below:

(1) Our WCE motion tracking algorithm in large intestine works with higher accuracy and stability when comparing with other algorithms published in the literature. Besides, our tracking algorithm works uniformly throughout the test with a wide range of rotation angles and relative displacements.

(2) The measurement errors of TOA based ranging inside human body could reach mm level (up to around 0.5mm) if appropriate estimation method is applied. And the

non-homogeneity is the main source of TOA ranging errors in in-body to surface channel.

(3) PDOA based ranging method does expand the maximum ranging distance comparing with TOA based ranging methods and it performs closely to that of TOA. The error of PDOA based method could also reach up to mm level (up to around 0.7mm).

6.2 Future Directions

Our work is still on the way which we might extend it in the future. The future work includes several aspects:

(a) Refine our visual motion tracking algorithm to be compatible with animation of GI tract.

(b) Reconstruct the GI tract using images emitted from WCE to help physician obtain more knowledge of their patients.

(c) combine the proposed tracking and ranging methods to come up with a novel hybrid localization approach.

Appendix A

Core code

A.1 Mutual information computation

```
function [mi] = Micounter(handles1,handles2)
a=handles1;
b=handles2;
[Ma,Na] = size(a);
[Mb,Nb] = size(b);
M=min(Ma,Mb);
N=min(Na,Nb);
 hab= zeros(256,256);
  ha= zeros(1,256);
  hb= zeros(1,256);
  if max(max(a))~=min(min(a))
  a = (a-min(min(a)))/(max(max(a))-min(min(a)));
 else
  a = zeros(M,N);
```

```
end
if max(max(b))~=min(min(b))
b = (b-min(min(b)))/(max(max(b))-min(min(b)));
else
b = zeros(M,N);
end
a = double(int16(a*255))+1;
b = double(int16(b*255))+1;
for i=1:M
for j=1:N
indexx= a(i,j);
indexy= b(i,j);
hab(indexx,indexy) = hab(indexx,indexy)+1;
ha(indexx) = ha(indexx)+1;
hb(indexy) = hb(indexy)+1;
end
end
hsum= sum(sum(hab));
index = find(hab~=0);
p = hab/hsum;
Hab= sum(sum(-p(index).*log(p(index))));
hsum= sum(sum(ha));
index = find(ha~=0);
p = ha/hsum;
Ha = sum(sum(-p(index).*log(p(index))));
hsum= sum(sum(hb));
```

```
index = find(hb~=0);
p = hb/hsum;
Hb= sum(sum(-p(index).*log(p(index))));
mi = Ha+Hb-Hab;
```

A.2 Fibonacci search

```
function [final_point,final_mi,difference]=...
gold_search1(start_point,direction,min,max,handles)
a=min;
b=max;
error=0.01;
T=0.618;
c=a+(1-T)*(b-a);
d=a+T*(b-a);
Fa=Fp(a,start_point,direction,handles);
Fb=Fp(b,start_point,direction,handles);
while(abs(b-a)>=error)
    if Fa<Fb
        a=c;
        b=b;
        c=a+(1-T)*(b-a);
        d=a+T*(b-a);
        Fa=Fp(a,start_point,direction,handles);
    else
        a=a;
```

```
            b=d;
            d=a+T*(b-a);
            c=a+(1-T)*(b-a);
            Fb=Fp(b,start_point,direction,handles);
        end
    end
    final_difference=(a+b)/2;
    final_point=start_point+final_difference*direction
    final_mi=Fp(final_difference,start_point,direction,handles)
    difference=final_difference;
```

A.3 Image rotation and bicubic interpolation

```
function I = Image_Rotate(handles,ang)
rad=pi/180*ang;
oldimage=handles;
[width,height]=size(oldimage);
newimage=uint8(zeros(width,height));
a=round((width-1)/2+0.5);
b=round((height-1)/2+0.5);
c=a;
d=b;

T1=[1 0 0;0 1 0;-a -b 1];
T2=[cos(rad) -sin(rad) 0;sin(rad) cos(rad) 0;0 0 1];
T3=[1 0 0;0 1 0;c d 1];
```

```
T=T1*T2*T3;
tform=maketform('affine',T);

tx=zeros(width,height);
ty=zeros(width,height);
for i=1:1:width
    for j=1:1:height
        tx(i,j)=i;
        ty(i,j)=j;
    end
end

[u v]=tforminv(tform,tx,ty);

for i=1:1:width
    for j=1:1:height
        source_x=u(i,j);
        source_y=v(i,j);
        if (source_x>=width-1||source_y>=height-1...
    ||double(uint8(source_x))<=0||double(uint8(source_y))
      <=0)
            newimage(i,j)=0;
%           else
%           if((source_x/double(uint8(source_x))==1)...
        &&(source_y/double(uint8(source_y))==1))
%                   newimage(i,j)=oldimage...
```

```
            ((int8(source_x)),(int8(source_y)));
            else
                a=double(int16(source_x));
                b=double(int16(source_y));
                x11=double(oldimage(a,b));
                x12=double(oldimage(a,b+1));
                x21=double(oldimage(a+1,b));
                x22=double(oldimage(a+1,b+1));
                newimage(i,j)=uint8((b+1-source_y)...
                *((source_x-a)*x21+(a+1-source_x)*x11)+...
                    (source_y-b)*((source_x-a)*x22+...
                    (a+1-source_x)*x12));
            end
%             end
        end
    end
    I=newimage;
```

A.4 CRLB calculation and TOA ranging methods

```
clear
clc
for cycle=1:10
%%
syms t w tau A
T0=2.5e-8;
```

```
SNR=1000;
W=1e10;
c=3e8;

I_s=A^2*(sin(2*t*w)+2*t*w)/(4*w);
I_tau=0.5*A^2*w^2*t-0.25*A^2*w*sin(2*w*(t-tau));

I_s=subs(I_s,A,1);
I_s=subs(I_s,t,T0)-subs(I_s,t,0);
I_s=subs(I_s,w,402e6)

I_tau=subs(I_tau,A,1);
I_tau=subs(I_tau,t,T0)-subs(I_tau,t,0);
I_tau=subs(I_tau,w,402e6)

k=1;
for tau=1e-9:1e-11:3*1e-9
    down=sin(296623644705249576562 5/14757395258967641292 8)
        ...
    /1608000000 + 9444732965739 29/7555786372591432341913 6;
    up=100500000*sin(804000000*tau -
        29662364470524957656 25/...
    14757395258967641292 8) - 100500000*sin(804000000*tau)
        +...
     9315836341524244513916015625/4611686018427387904;
    F=2*SNR*W*T0*up/down;
```

```
    crlb(k)=1/sqrt(F)*c/sqrt(27.9);
    k=k+1;

end
tau=1e-9:1e-11:3*1e-9;
 plot(tau*3e8/sqrt(27.9)*1000,crlb*1000),xlim([57  171]);
%  ylim([0, 2]);
 hold on
 xlabel('distance/mm'), ylabel('ranging error/mm')


%% gcc
imported_data=importdata('inbody_27.9.mat');
str1='imported_data.source';
str2='imported_data.sensor';
for count= 1:100
for j=1:7
    if (j==2)||(j==3)||(j==4)||(j==7)
source=eval(str1);
sensor=eval([str2,num2str(j)]);
Fs=1/(sensor(3,1)-sensor(2,1));
start=0;
for i=1:length(sensor)
    if sensor(i,1)>=6e-9
        start=i;
        break
```

```
    end
end
t=sensor(start:length(sensor),1);
x=source(start:length(sensor),2);
amp=max(source(:,2))/max(sensor(:,2));
y=-amp*sensor(start:length(sensor),2);
x=awgn(x,30);
y=awgn(y,30);
N=length(y);
% figure(1)
% subplot(2,1,1),plot(t,x)
% subplot(2,1,2),plot(t,y)

X=fft(x,2*N-1);
Y=fft(y,2*N-1);
gcc=X.*conj(Y);
% G=abs(X).*abs(Y);
% gcc=gcc./G;
gcc=fftshift(ifft(gcc));
% gcc=abs(gcc);

lags=-N+1:1:N-1;      %??????
% figure
% subplot(211),plot(lags/Fs,gcc),title('gcc'),grid on;
[c,lags]=xcorr(x,y);
% subplot(212),plot(lags/Fs,c,'r'),title('xcorr'),grid on;
```

```
for i=-10:10
    index(i+11)=lags(find(c==max(c))+i);
    value(i+11)=c(find(c==max(c))+i);
end
interpolated_index=index(1):0.001:index(length(index));
interpolated_value=interp1(index,value,interpolated_index,'
   spline');
delay(j)=interpolated_index(find(interpolated_value...
==max(interpolated_value)))/Fs;
time_delay=1/402e6-abs(delay(j));
% time_delay=abs(delay(j));
distance(count,j)=time_delay*3e8/sqrt(27.9)*1000;
actual_distance(count,:)=[75.948 98.951 120.637 134.231];
    end
end
end

x=[actual_distance(:,1); actual_distance(:,2); ...
actual_distance(:,3); actual_distance(:,4)];
y=[distance(:,2); distance(:,3); distance(:,4); distance
   (:,7)];
error=sum(x-y)/length(x);
y=y+error;
error=abs(y-x);
error_mean=zeros(1,4);
error_mean_gcc(cycle,1)=sum(error(1:100))/length(error
```

```
    (1:100));
error_mean_gcc(cycle,2)=sum(error(101:200))/length(error
    (101:200));
error_mean_gcc(cycle,3)=sum(error(201:300))/length(error
    (201:300));
error_mean_gcc(cycle,4)=sum(error(301:400))/length(error
    (301:400));
plot(actual_distance(1,:),error_mean_gcc(cycle,:),'*'),...
 grid on, hold on


%% all peaks
c=3e8;
epsilon_blood=27.9;
imported_data=importdata('inbody_27.9.mat');

for count=1:100
[peak_source, time_peak_source, peak_received,
    time_peak_received]...
= PeakDetection(imported_data.sensor2,imported_data.source)
    ;
for i=1:length(time_peak_received)
    time_difference(i)=abs(time_peak_received(i)-
        time_peak_source(i));
    measured_distance(i)=time_difference(i)*c/sqrt(
        epsilon_blood);
```

```
end
mean_distance1(count)=sum(measured_distance)...
/length(measured_distance)*1000;


[peak_source, time_peak_source, peak_received,
   time_peak_received]...
= PeakDetection(imported_data.sensor3,imported_data.source)
   ;
for i=1:length(time_peak_received)
    time_difference(i)=abs(time_peak_received(i)-
       time_peak_source(i));
    measured_distance(i)=time_difference(i)*c/sqrt(
       epsilon_blood);
end
mean_distance2(count)=sum(measured_distance)/...
length(measured_distance)*1000;


[peak_source, time_peak_source, peak_received,
   time_peak_received] ...
= PeakDetection(imported_data.sensor4,imported_data.source)
   ;
for i=1:length(time_peak_received)
    time_difference(i)=abs(time_peak_received(i)...
    -time_peak_source(i));
```

```
    measured_distance(i)=time_difference(i)*c/sqrt(
        epsilon_blood);
end
mean_distance3(count)=sum(measured_distance)/...
length(measured_distance)*1000;



[peak_source, time_peak_source, peak_received,
    time_peak_received]...
= PeakDetection(imported_data.sensor7,imported_data.source)
    ;
for i=1:length(time_peak_received)
    time_difference(i)=abs(time_peak_received(i)-
        time_peak_source(i));
    measured_distance(i)=time_difference(i)*c/sqrt(
        epsilon_blood);
end
mean_distance4(count)=sum(measured_distance)/...
length(measured_distance)*1000;

actual_distance(count,:)=[75.948 98.951 120.637 134.231];
end
x=[actual_distance(:,1); actual_distance(:,2);
    actual_distance(:,3);...
 actual_distance(:,4)];
```

```
y=[mean_distance1'; mean_distance2'; mean_distance3';
    mean_distance4'];
error=sum(x-y)/length(x);
y=y+error;
error=abs(y-x);
error_mean=zeros(1,4);
error_mean_dap(cycle,1)=sum(error(1:100))/length(error
    (1:100));
error_mean_dap(cycle,2)=sum(error(101:200))/length(error
    (101:200));
error_mean_dap(cycle,3)=sum(error(201:300))/length(error
    (201:300));
error_mean_dap(cycle,4)=sum(error(301:400))/length(error
    (301:400));
plot(actual_distance(1,:),error_mean_dap(cycle,:),'ro'),
    ...
grid on, hold on

%% first peak

c=3e8;
epsilon_blood=27.9;
imported_data=importdata('inbody_27.9.mat');

for count=1:100
[peak_source, time_peak_source, peak_received,
```

```
    time_peak_received]...
= PeakDetection(imported_data.sensor2,imported_data.source)
    ;
time_difference=abs(time_peak_received(1)-time_peak_source
    (1));
measured_distance=time_difference*c/sqrt(epsilon_blood);
mean_distance1(count)=measured_distance*1000;



[peak_source, time_peak_source, peak_received,
    time_peak_received]...
= PeakDetection(imported_data.sensor3,imported_data.source)
    ;
time_difference=abs(time_peak_received(1)-time_peak_source
    (1));
measured_distance=time_difference*c/sqrt(epsilon_blood);
mean_distance2(count)=measured_distance*1000;


[peak_source, time_peak_source, peak_received,
    time_peak_received]...
= PeakDetection(imported_data.sensor4,imported_data.source)
    ;
time_difference=abs(time_peak_received(1)-time_peak_source
    (1));
```

```
measured_distance=time_difference*c/sqrt(epsilon_blood);
mean_distance3(count)=measured_distance*1000;



[peak_source, time_peak_source, peak_received,
    time_peak_received]...
= PeakDetection(imported_data.sensor7,imported_data.source)
    ;
time_difference=abs(time_peak_received(1)-time_peak_source
    (1));
measured_distance=time_difference*c/sqrt(epsilon_blood);
mean_distance4(count)=measured_distance*1000;

actual_distance(count,:)=[75.948 98.951 120.637 134.231];
end
x=[actual_distance(:,1); actual_distance(:,2);...
 actual_distance(:,3); actual_distance(:,4)];
y=[mean_distance1'; mean_distance2'; mean_distance3';
    mean_distance4'];
error=sum(x-y)/length(x);
y=y+error;
error=abs(y-x);
% plot(x,y,'*');
% hold on
% plot([75.948 98.951 120.637 134.231],...
```

```
[75.948 98.951 120.637 134.231],'ro')
% error_mean=sum(error)/length(error)
% figure
% plot(x,error,'*')
error_mean=zeros(1,4);
error_mean_dfp(cycle,1)=sum(error(1:100))/length(error
    (1:100));
error_mean_dfp(cycle,2)=sum(error(101:200))/length(error
    (101:200));
error_mean_dfp(cycle,3)=sum(error(201:300))/length(error
    (201:300));
error_mean_dfp(cycle,4)=sum(error(301:400))/length(error
    (301:400));
plot(actual_distance(1,:),error_mean_dfp(cycle,:),'m+'),
    ...
grid on, hold on
legend('Bound for TOA ranging error','Generalized Cross...
 Correlation','Detection of All Peaks','Detection of First
    Peak')
end
actual_distance(1,:)

for k=1:4
     y_gcc(k)=sum(error_mean_gcc(:,k))/10;
     e_gcc(k)=max(error_mean_gcc(:,k))-min(error_mean_gcc(:,
        k));
```

```
    y_dap(k)=sum(error_mean_dap(:,k))/10;
    e_dap(k)=max(error_mean_dap(:,k))-min(error_mean_dap(:,
        k));

    y_dfp(k)=sum(error_mean_dfp(:,k))/10;
    e_dfp(k)=max(error_mean_dfp(:,k))-min(error_mean_dfp(:,
        k));
end
errorbar(actual_distance(1,:),y_gcc,e_gcc/2)
errorbar(actual_distance(1,:),y_dap,e_dap/2)
errorbar(actual_distance(1,:),y_dfp,e_dfp/2)
```

Appendix B

Brief tutorial to Simulations

B.1 Tutorial to FDTD algorithm

In this thesis, all simulations are conducted using three dimensional Finite Difference Time Domain (FDTD) [93] solver with the Yee algorithm [94] (shown in Figure B.1).

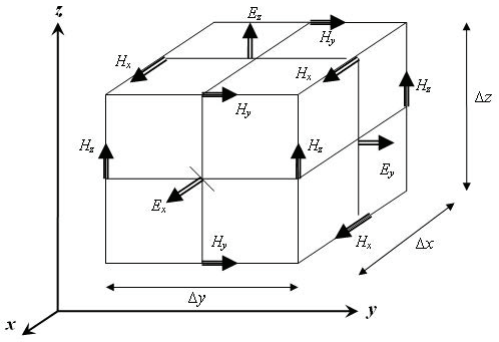

Figure B.1: The 3-D model of Yee Algorithm

In the Yee algorithm, consider $\frac{\partial H_x}{\partial t} = \frac{1}{\mu}(\frac{\partial E_y}{\partial z} - \frac{\partial E_z}{\partial y})$, then using central differential equation we have

$$\frac{H_x^{n+1/2}(i,j,k) - H_x^{n-1/2}(i,j,k)}{\Delta t} = \frac{1}{\mu(i,j,k)}[\frac{E_y^n(i,j,k+1/2) - E_y^n(i,j,k-1/2)}{\Delta z} - \frac{E_z^n(i,j+1/2,k) - E_z^n(i,j-1/2,k)}{\Delta y}] \tag{B.1}$$

where $\mu(i,j,k)$ denotes the permeability at specific point. Equation B.1 therefore defines the relationship of $H_x(i,j,k)$ at time step $n+1/2$ and that at time step $n-1/2$. Thus we come to Equation B.2:

$$H_x^{n+1/2}(i,j,k) = H_x^{n-1/2}(i,j,k) + \frac{\Delta t}{\mu(i,j,k)}[\frac{E_y^n(i,j,k+1/2) - E_y^n(i,j,k-1/2)}{\Delta z} - \frac{E_z^n(i,j+1/2,k) - E_z^n(i,j-1/2,k)}{\Delta y}] \tag{B.2}$$

Now consider $\frac{\partial E_x}{\partial t} = \frac{1}{\varepsilon}(\frac{\partial H_z}{\partial y} - \frac{\partial H_y}{\partial z} - \sigma E_x)$, if we apply the similar steps in Equation B.1 and B.2, then we have

$$\frac{E_x^{n+1}(i,j,k) - E_x^n(i,j,k)}{\Delta t} = \frac{1}{\varepsilon(i,j,k)}[\frac{H_z^{n+1/2}(i,j+1/2,k) - E_z^{n+1/2}(i,j-1/2,k)}{\Delta y} - \frac{H_y^{n+1/2}(i,j,k+1/2) - H_y^{n+1/2}(i,j,k-1/2)}{\Delta z}] - \frac{\varepsilon(i,j,k)}{\sigma(i,j,k)} E_x^{n+1/2}(i,j,k) \tag{B.3}$$

Plug in central differential equation $E_x^{n+1/2}(i,j,k) \simeq \frac{E_x^{n+1}(i,j,k) + E_x^n(i,j,k)}{2}$ we have

$$E_x^{n+1}(i,j,k) = \frac{1-\frac{\Delta t\sigma(i,j,k)}{2\varepsilon(i,j,k)}}{1+\frac{\Delta t\sigma(i,j,k)}{2\varepsilon(i,j,k)}} E_x^n(i,j,k) +$$
$$\frac{\frac{\Delta t}{\varepsilon(i,j,k)}}{\varepsilon(i,j,k)}\left[\frac{H_z^{n+1/2}(i,j+1/2,k)-E_z^{n+1/2}(i,j-1/2,k)}{\Delta y} - \right. \tag{B.4}$$
$$\left.\frac{H_y^{n+1/2}(i,j,k+1/2)-H_y^{n+1/2}(i,j,k-1/2)}{\Delta z}\right] - \frac{\varepsilon(i,j,k)}{\sigma(i,j,k)} E_x^{n+1/2}(i,j,k)$$

Equation B.2 and B.4 can be more clearly if you take a glance at Figure B.2.

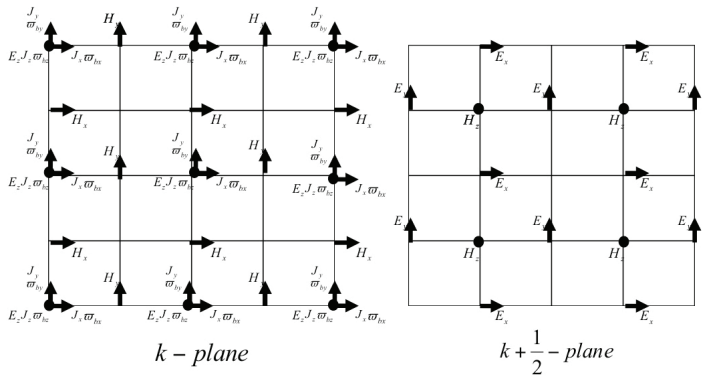

Figure B.2: The expanded Yee cell with k-plane and k+1/2-plane

Now the relationships between consecutive steps are clear.

B.1.1 Tutorial to SEMCAD X

SEMCAD was originally started through various projects at ETH in Zurich. It is setting new standards in computational electromagnetic (CEM) software, being the most efficient, functionally complete and affordable toolsets for antenna design and general EM/Thermal simulation on the market [95].

To help readers come up with a smoother reading experience of the simulation part in this thesis, a brief tutorial of SEMCAD X is posted in this subsection.

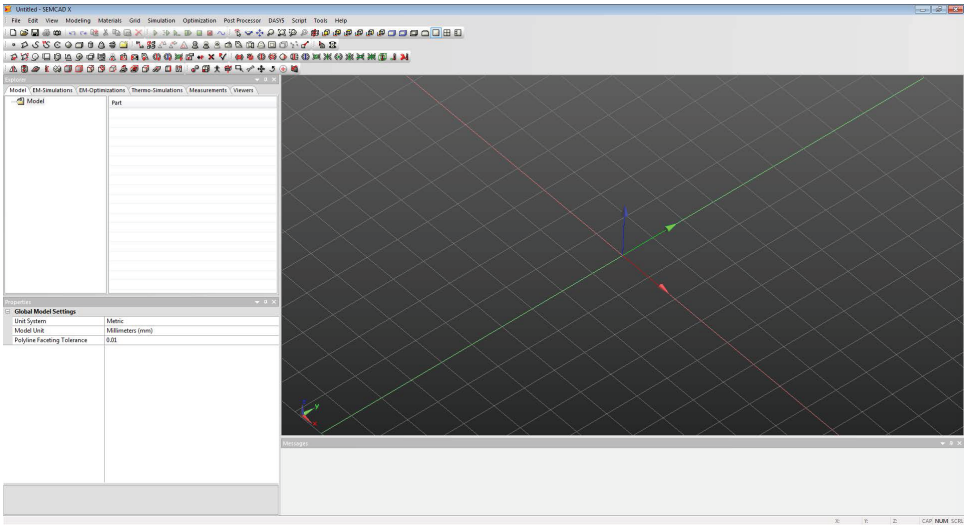

Figure B.3: The main interface of SEMCAD X

Figure B.3 shows the main interface of SEMCAD X 14.8. This interface will automatically show up after we start the server which is usually a workstation or desktop. SEMCAD X provides users with a family of human phantom containing detailed organ tissue materials to conduct accurate CEM simulations.

To run simulations on SEMCAD X, we provide instructions with figures below to present a full procedure of a simulation.

First, we import the phantom or other models to SEMCAD X main GUI. File $\rightarrow$ Import Model $\rightarrow$ select the model type and model file you need to import. After import is done, the model will show up in Main GUI. A sample of this operation is given in Figure B.4.

Second, in the ”explorer” frame, we can edit the model as well as add or delete other objects. To edit the other configurable settings such as signal frequency, grid size, time step and etc, we can refer to the frame ”EM-Simulations”, as shown in Figure B.5

Then, we right click the ”Grid” item and select ”Lock Grid” operation, and click ”Run Simulation”.

Finally after the simulation is done, we open ”Result” in ”EM-Simulation”, and send

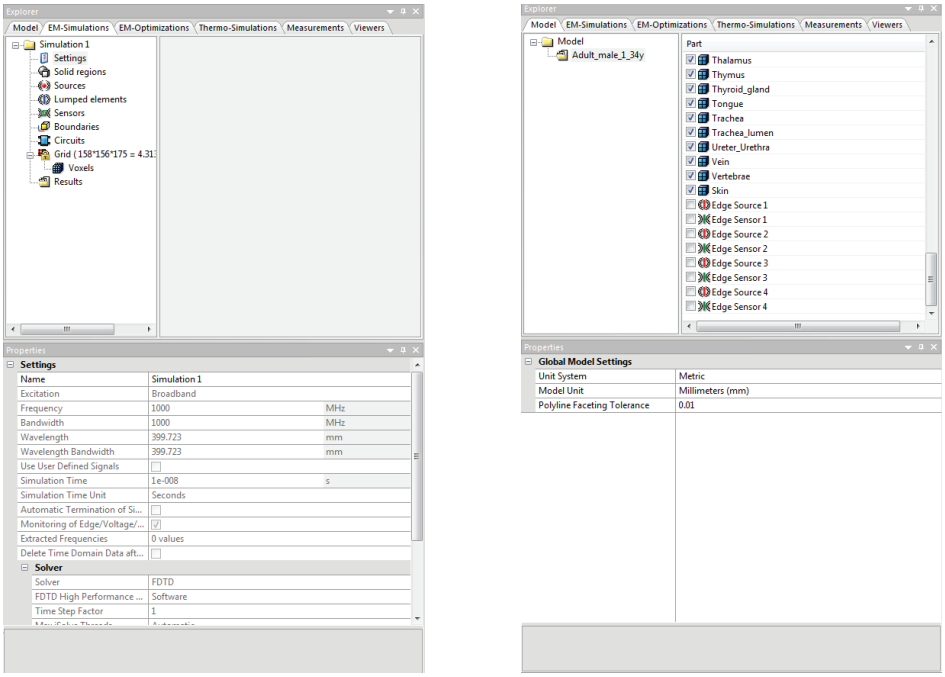

(a) (b)

Figure B.4: (a) Frame ”Explorer” to edit the model; (b) Frame ”EM-Simulation” to configure the settings of simulation

what we need to Viewers. Figure B.6 shows a sample of the simulation results.

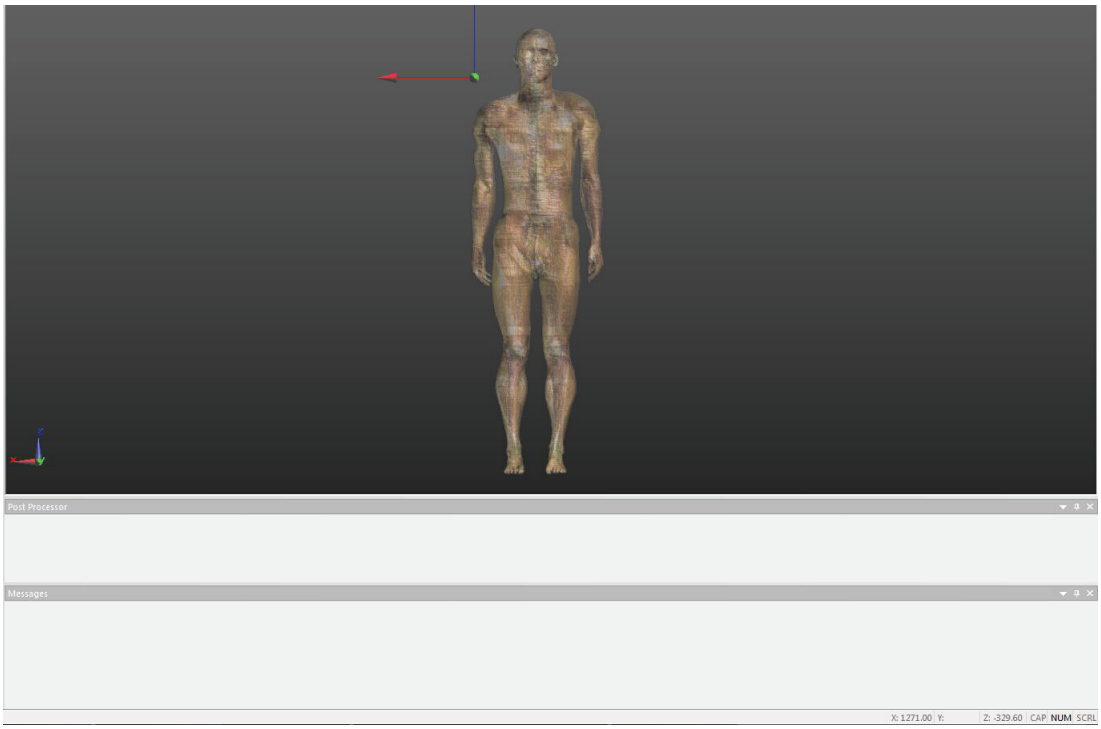

Figure B.5: A sample of received signal voltage from simulation results

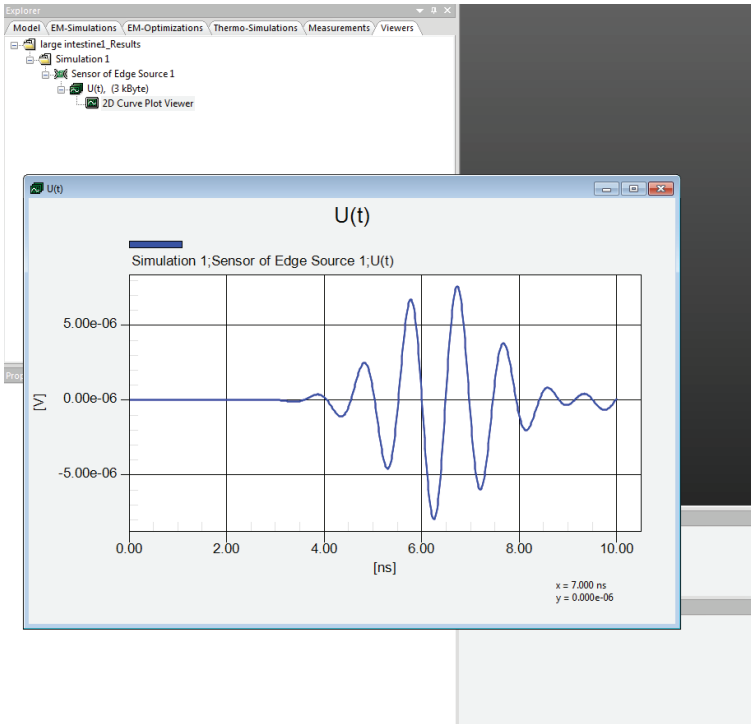

Figure B.6: A sample of received signal voltage from simulation results

Bibliography

[1] K. S. Kwak, S. Ullah, and N. Ullah, "An overview of ieee 802.15. 6 standard," in *Applied Sciences in Biomedical and Communication Technologies (ISABEL), 2010 3rd International Symposium on*. IEEE, 2010, pp. 1–6.

[2] F. Martelli, C. Buratti, and R. Verdone, "On the performance of an ieee 802.15. 6 wireless body area network," in *Wireless Conference 2011-Sustainable Wireless Technologies (European Wireless), 11th European*. VDE, 2011, pp. 1–6.

[3] B. Latré, B. Braem, I. Moerman, C. Blondia, and P. Demeester, "A survey on wireless body area networks," *Wireless Networks*, vol. 17, no. 1, pp. 1–18, 2011.

[4] M. Zhou, G. Bao, and K. Pahlavan, "Measurement of motion detection of wireless capsule endoscope inside large intestine," in *Engineering in Medicine and Biology Society (EMBC), 2014 36th Annual International Conference of the IEEE*. IEEE, 2014, pp. 5591–5594.

[5] G. Iddan, G. Meron, A. Glukhovsky, and P. Swain, "Wireless capsule endoscopy," *Nature*, vol. 405, no. 6785, pp. 417–417, 2000.

[6] T. D. Than, G. Alici, H. Zhou, and W. Li, "A review of localization systems for robotic endoscopic capsules," *Biomedical Engineering, IEEE Transactions on*, vol. 59, no. 9, pp. 2387–2399, 2012.

[7] E. Spyrou and D. K. Iakovidis, "Homography-based orientation estimation for capsule endoscope tracking," in *Imaging Systems and Techniques (IST), 2012 IEEE International Conference on*. IEEE, 2012, pp. 101–105.

[8] D. K. Iakovidis, E. Spyrou, D. Diamantis, and I. Tsiompanidis, "Capsule endoscope localization based on visual features," in *Bioinformatics and Bioengineering (BIBE), 2013 IEEE 13th International Conference on*. IEEE, 2013, pp. 1–4.

[9] L. Liu, C. Hu, W. Cai, and M.-H. Meng, "Capsule endoscope localization based on computer vision technique," in *Engineering in Medicine and Biology Society, 2009. EMBC 2009. Annual International Conference of the IEEE*. IEEE, 2009, pp. 3711–3714.

[10] P. Swar, K. Pahlavan, and U. Khan, "Accuracy of localization system inside human body using a fast fdtd simulation technique," in *Medical Information and Communication Technology (ISMICT), 2012 6th International Symposium on*. IEEE, 2012, pp. 1–6.

[11] Z. Liu, J. Chen, U. Khan, B. Alkandari, and K. Pahlavan, "Wideband characterization of rf propagation for toa localization of wireless video capsule endoscope inside small intestine," in *Personal Indoor and Mobile Radio Communications (PIMRC), 2013 IEEE 24th International Symposium on*. IEEE, 2013, pp. 326–331.

[12] A. Povalac and J. Sebesta, "Phase difference of arrival distance estimation for rfid tags in frequency domain," in *RFID-Technologies and Applications (RFID-TA), 2011 IEEE International Conference on*. IEEE, 2011, pp. 188–193.

[13] C. NEZHAT and C. NEZHAT, "Operative laparoscopy (minimally invasive surgery): state of the art," *Journal of gynecologic surgery*, vol. 8, no. 3, pp. 111–141, 1992.

[14] S. J. SPANER and G. L. WARNOCK, "A brief history of endoscopy, laparoscopy, and laparoscopic surgery," *Journal of Laparoendoscopic & Advanced Surgical Techniques*, vol. 7, no. 6, pp. 369–373, 1997.

[15] S. Banerjee, "Begining of endoscopy," *Indian Journal of Otolaryngology and Head & Neck Surgery*, vol. 47, no. 3, pp. 171–172, 1995.

[16] D. A. Lieberman, D. G. Weiss, J. H. Bond, D. J. Ahnen, H. Garewal, W. V. Harford, D. Provenzale, S. Sontag, T. Schnell, T. E. Durbin *et al.*, "Use of colonoscopy to screen asymptomatic adults for colorectal cancer," *New England Journal of Medicine*, vol. 343, no. 3, pp. 162–168, 2000.

[17] L. E. Moore, "The advantages and disadvantages of endoscopy," *Clinical techniques in small animal practice*, vol. 18, no. 4, pp. 250–253, 2003.

[18] C. Hassan and A. Zullo, "Capsule endoscopy versus colonoscopy," *N Engl J Med*, vol. 361, no. 3, pp. 264–70, 2009.

[19] A. Van Gossum, M. Munoz-Navas, I. Fernandez-Urien, C. Carretero, G. Gay, M. Delvaux, M. G. Lapalus, T. Ponchon, H. Neuhaus, M. Philipper *et al.*, "Capsule endoscopy versus colonoscopy for the detection of polyps and cancer," *New England Journal of Medicine*, vol. 361, no. 3, pp. 264–270, 2009.

[20] D. Hartmann, D. Schilling, G. Bolz, M. Hahne, R. Jakobs, E. Siegel, U. Weickert, H. Adamek, and J. Riemann, "Capsule endoscopy versus push enteroscopy in patients with occult gastrointestinal bleeding." *Zeitschrift fur Gastroenterologie*, vol. 41, no. 5, pp. 377–382, 2003.

[21] G. J. Iddan and C. P. Swain, "History and development of capsule endoscopy," *Gastrointestinal endoscopy clinics of North America*, vol. 14, no. 1, pp. 1–9, 2004.

[22] N. Schoofs, J. Devière, and A. Van Gossum, "Pillcam colon capsule endoscopy compared with colonoscopy for colorectal tumor diagnosis: a prospective pilot study." *Endoscopy*, vol. 38, no. 10, pp. 971–977, 2006.

[23] M.-H. Meng, T. Mei, J. Pu, C. Hu, X. Wang, and Y. Chan, "Wireless robotic capsule endoscopy: state-of-the-art and challenges," in *Intelligent Control and Automation, 2004. WCICA 2004. Fifth World Congress on*, vol. 6. IEEE, 2004, pp. 5561–555a.

[24] M. Keroack, "Video capsule endoscopy," *Current opinion in gastroenterology*, vol. 20, no. 5, pp. 474–481, 2004.

[25] T. D. Wang, "A novel capsule endoscope: do we need new kids on the block?" *Gastrointestinal endoscopy*, vol. 69, no. 2, p. 260, 2009.

[26] M. Yu, "M2a capsule endoscopy: A breakthrough diagnostic tool for small intestine imaging," *Gastroenterology Nursing*, vol. 25, no. 1, pp. 24–27, 2002.

[27] B. S. Lewis and P. Swain, "Capsule endoscopy in the evaluation of patients with suspected small intestinal bleeding: results of a pilot study," *Gastrointestinal endoscopy*, vol. 56, no. 3, pp. 349–353, 2002.

[28] C. Gheorghe, R. Iacob, I. Bancila *et al.*, "Olympus capsule endoscopy for small bowel examination," *Journal of Gastrointestinal and Liver Diseases*, vol. 16, no. 3, p. 309, 2007.

[29] A. Sieg, K. Friedrich, and U. Sieg, "Is pillcam colon capsule endoscopy ready for colorectal cancer screening? a prospective feasibility study in a community gastroenterology practice," *The American journal of gastroenterology*, vol. 104, no. 4, pp. 848–854, 2009.

[30] G. Bao, "On simultaneous localization and mapping inside the human body (bodyslam)," Ph.D. dissertation, Worcester Polytechnic Institute, 2014.

[31] C. Spada, C. Hassan, M. Munoz-Navas, H. Neuhaus, J. Deviere, P. Fockens, E. Coron, G. Gay, E. Toth, M. E. Riccioni *et al.*, "Second-generation colon capsule endoscopy compared with colonoscopy," *Gastrointestinal endoscopy*, vol. 74, no. 3, pp. 581–589, 2011.

[32] G. Gay, M. Delvaux, and J. Rey, "The role of video capsule endoscopy in the diagnosis of digestive diseases: a review of current possibilities." *Endoscopy*, vol. 36, no. 10, pp. 913–920, 2004.

[33] R. Eliakim, Z. Fireman, I. Gralnek, K. Yassin, M. Waterman, Y. Kopelman, J. Lachter, B. Koslowsky, and S. Adler, "Evaluation of the pillcam colon capsule in the detection of colonic pathology: results of the first multicenter, prospective, comparative study." *Endoscopy*, vol. 38, no. 10, pp. 963–970, 2006.

[34] P. R. Slawinski, K. L. Obstein, and P. Valdastri, "Emerging issues and future developments in capsule endoscopy," *Techniques in Gastrointestinal Endoscopy*, 2015.

[35] D. G. Adler and C. J. Gostout, "Wireless capsule endoscopy," *Hospital Physician*, vol. 39, no. 5, pp. 14–22, 2003.

[36] M. Zhou, G. Bao, Y. Geng, B. Alkandari, and X. Li, "Polyp detection and radius measurement in small intestine using video capsule endoscopy," in *Biomedical Engineering and Informatics (BMEI), 2014 7th International Conference on*. IEEE, 2014, pp. 237–241.

[37] K. Pahlavan, G. Bao, Y. Ye, S. Makarov, U. Khan, P. Swar, D. Cave, A. Karellas, P. Krishnamurthy, and K. Sayrafian, "Rf localization for wireless video capsule endoscopy," *International Journal of Wireless Information Networks*, vol. 19, no. 4, pp. 326–340, 2012.

[38] Y. Ye, P. Swar, K. Pahlavan, and K. Ghaboosi, "Accuracy of rss-based rf localization in multi-capsule endoscopy," *International Journal of Wireless Information Networks*, vol. 19, no. 3, pp. 229–238, 2012.

[39] M. Kawasaki and R. Kohno, "A toa based positioning technique of medical implanted devices," in *Third International Symposium on Medical Information & Communication Technology, ISMCIT09, Montreal*, 2009.

[40] R. Chandra, A. J. Johansson, and F. Tufvesson, "Localization of an rf source inside the human body for wireless capsule endoscopy," in *Proceedings of the 8th International Conference on Body Area Networks*. ICST (Institute for Computer Sciences, Social-Informatics and Telecommunications Engineering), 2013, pp. 48–54.

[41] G. Bao, Y. Ye, U. Khan, X. Zheng, and K. Pahlavan, "Modeling of the movement of the endoscopy capsule inside gi tract based on the captured endoscopic images," in *Proceedings of the IEEE International Conference on Modeling, Simulation and Visualization Methods, MSV*, vol. 12, 2012.

[42] A. Karargyris and N. Bourbakis, "Wireless capsule endoscopy and endoscopic imaging: A survey on various methodologies presented," *Engineering in Medicine and Biology Magazine, IEEE*, vol. 29, no. 1, pp. 72–83, 2010.

[43] A. Hatami and K. Pahlavan, "Performance comparison of rss and toa indoor geolocation based on uwb measurement of channel characteristics," in *Personal, Indoor and Mobile Radio Communications, 2006 IEEE 17th International Symposium on*. IEEE, 2006, pp. 1–6.

[44] K. R. Foster and H. P. Schwan, "Dielectric properties of tissues and biological materials: a critical review." *Critical reviews in biomedical engineering*, vol. 17, no. 1, pp. 25–104, 1988.

[45] Y. Geng, "Modeling of time-of-arrival for cm4 body area networks channel," Ph.D. dissertation, Worcester Polytechnic Institute, 2013.

[46] K. Ho and Y. Chan, "Solution and performance analysis of geolocation by tdoa," *Aerospace and Electronic Systems, IEEE Transactions on*, vol. 29, no. 4, pp. 1311–1322, 1993.

[47] F. Gustafsson and F. Gunnarsson, "Positioning using time-difference of arrival measurements," in *Acoustics, Speech, and Signal Processing, 2003. Proceedings.(ICASSP'03). 2003 IEEE International Conference on*, vol. 6. IEEE, 2003, pp. VI–553.

[48] X. Li, "Rss-based location estimation with unknown pathloss model," *Wireless Communications, IEEE Transactions on*, vol. 5, no. 12, pp. 3626–3633, 2006.

[49] K. Sayrafian-Pour, W.-B. Yang, J. Hagedorn, J. Terrill, and K. Y. Yazdandoost, "A statistical path loss model for medical implant communication channels," in *Personal, Indoor and Mobile Radio Communications, 2009 IEEE 20th International Symposium on*. IEEE, 2009, pp. 2995–2999.

[50] H.-B. Li and R. Kohno, "Body area network and its standardization at ieee 802.15. ban," in *Advances in Mobile and Wireless Communications*. Springer, 2008, pp. 223–238.

[51] M. Bouet and A. L. Dos Santos, "Rfid tags: Positioning principles and localization techniques," in *Wireless Days, 2008. WD'08. 1st IFIP*. IEEE, 2008, pp. 1–5.

[52] G. Bao and K. Pahlavai, "Motion estimation of the endoscopy capsule using region-based kernel svm classifier," in *Electro/Information Technology (EIT), 2013 IEEE International Conference on*. IEEE, 2013, pp. 1–5.

[53] D. Murray and A. Basu, "Motion tracking with an active camera," *Pattern Analysis and Machine Intelligence, IEEE Transactions on*, vol. 16, no. 5, pp. 449–459, 1994.

[54] J. P. Pluim, J. A. Maintz, and M. A. Viergever, "Mutual-information-based registration of medical images: a survey," *Medical Imaging, IEEE Transactions on*, vol. 22, no. 8, pp. 986–1004, 2003.

[55] P. Viola and W. M. Wells III, "Alignment by maximization of mutual information," *International journal of computer vision*, vol. 24, no. 2, pp. 137–154, 1997.

[56] G. Ciuti, A. Menciassi, and P. Dario, "Capsule endoscopy: from current achievements to open challenges," *Biomedical Engineering, IEEE Reviews in*, vol. 4, pp. 59–72, 2011.

[57] G. Bao, L. Mi, and K. Pahlavan, "A video aided rf localization technique for the wireless capsule endoscope (wce) inside small intestine," in *Proceedings of the 8th International Conference on Body Area Networks*. ICST (Institute for Computer Sciences, Social-Informatics and Telecommunications Engineering), 2013, pp. 55–61.

[58] ——, "Emulation on motion tracking of endoscopic capsule inside small intestine," in *14th International Conference on Bioinformatics and Computational Biology, Las Vegas*, 2013.

[59] E. Spyrou and D. K. Iakovidis, "Video-based measurements for wireless capsule endoscope tracking," *Measurement Science and Technology*, vol. 25, no. 1, p. 015002, 2014.

[60] T. Lindeberg, "Scale invariant feature transform," *Scholarpedia*, vol. 7, no. 5, p. 10491, 2012.

[61] S. N. Adler and Y. C. Metzger, "Pillcam colon capsule endoscopy: recent advances and new insights," *Therapeutic advances in gastroenterology*, vol. 4, no. 4, pp. 265–268, 2011.

[62] J. P. Pluim, J. A. Maintz, and M. A. Viergever, "Image registration by maximization of combined mutual information and gradient information," in *Medical Image Computing and Computer-Assisted Intervention–MICCAI 2000*. Springer, 2000, pp. 452–461.

[63] D. Fischer, R. Schreiber, D. Levi, and R. Eliakim, "Capsule endoscopy: the localization system," *Gastrointestinal endoscopy clinics of north america*, vol. 14, no. 1, pp. 25–31, 2004.

[64] R. C. Gonzalez, *Digital image processing*. Pearson Education India, 2009.

[65] A. Antoniou, *Digital signal processing*. McGraw-Hill Toronto, Canada:, 2006.

[66] C. E. Shannon, "A mathematical theory of communication," *ACM SIGMOBILE Mobile Computing and Communications Review*, vol. 5, no. 1, pp. 3–55, 2001.

[67] R. Battiti, "Using mutual information for selecting features in supervised neural net learning," *Neural Networks, IEEE Transactions on*, vol. 5, no. 4, pp. 537–550, 1994.

[68] W. H. Press, S. A. Teukolsky, W. T. Vetterling, and B. P. Flannery, "Golden section search in one dimension," *Numerical Recipies in C: the Art of Scientific Computing*, vol. 2, 1992.

[69] T. H. Cormen, C. E. Leiserson, R. L. Rivest, C. Stein *et al.*, *Introduction to algorithms*. MIT press Cambridge, 2001, vol. 2.

[70] I. Bankman, *Handbook of medical image processing and analysis*. academic press, 2008.

[71] D. Lancaster, "A review of some image pixel interpolation algorithms," *copyright c2007 as Guru Gram*, vol. 32, 2007.

[72] M. Pourhomayoun, M. Fowler, and Z. Jin, "A novel method for medical implant in-body localization," in *Engineering in Medicine and Biology Society (EMBC), 2012 Annual International Conference of the IEEE*. IEEE, 2012, pp. 5757–5760.

[73] G. Bao, K. Pahlavan, and L. Mi, "Hybrid localization of micro-robotic endoscopic capsule inside small intestine by data fusion of vision and rf sensors," 2014.

[74] U. I. Khan, K. Pahlavan, and S. Makarov, "Comparison of toa and rss based techniques for rf localization inside human tissue," in *Engineering in Medicine and Biology Society, EMBC, 2011 Annual International Conference of the IEEE*. IEEE, 2011, pp. 5602–5607.

[75] C. Radhakrishna Rao, "Information and accuracy attainable in the estimation of statistical parameters," *Bulletin of the Calcutta Mathematical Society*, vol. 37, no. 3, pp. 81–91, 1945.

[76] S. Li, Y. Geng, J. He, and K. Pahlavan, "Analysis of three-dimensional maximum likelihood algorithm for capsule endoscopy localization," in *Biomedical Engineering and Informatics (BMEI), 2012 5th International Conference on*. IEEE, 2012, pp. 721–725.

[77] D. R. Pauluzzi and N. C. Beaulieu, "A comparison of snr estimation techniques for the awgn channel," *Communications, IEEE Transactions on*, vol. 48, no. 10, pp. 1681–1691, 2000.

[78] H. L. Van Trees, *Detection, estimation, and modulation theory*. John Wiley & Sons, 2004.

[79] K. Pahlavan and P. Krishnamurthy, *Principles of Wireless Access and Localization*. John Wiley & Sons, 2013.

[80] G. Del Castillo, C. Mason, N. Chavannes, and M. Okoniewski, "High performance, high accuracy fdtd implementation on gpu architectures," *Microwave Engineering Europe*, 2010.

[81] M. Azaria and D. Hertz, "Time delay estimation by generalized cross correlation methods," *Acoustics, Speech and Signal Processing, IEEE Transactions on*, vol. 32, no. 2, pp. 280–285, 1984.

[82] S. Chen, Y. Ye, and K. Pahlavan, "Comparison of uwb and nb rf ranging measurements in homogenous tissue for ban applications," in *Wireless Telecommunications Symposium (WTS), 2013*. IEEE, 2013, pp. 1–5.

[83] M. Pourhomayoun, Z. Jin, and M. L. Fowler, "Accurate localization of in-body medical implants based on spatial sparsity," *Biomedical Engineering, IEEE Transactions on*, vol. 61, no. 2, pp. 590–597, 2014.

[84] A. Fort, J. Ryckaert, C. Desset, P. De Doncker, P. Wambacq, and L. Van Biesen, "Ultra-wideband channel model for communication around the human body," *Selected Areas in Communications, IEEE Journal on*, vol. 24, no. 4, pp. 927–933, 2006.

[85] T. Zasowski and A. Wittneben, "Performance of uwb receivers with partial csi using a simple body area network channel model," *Selected Areas in Communications, IEEE Journal on*, vol. 27, no. 1, pp. 17–26, 2009.

[86] N. Cho, J. Yoo, S.-J. Song, J. Lee, S. Jeon, and H.-J. Yoo, "The human body characteristics as a signal transmission medium for intrabody communication," *Microwave Theory and Techniques, IEEE Transactions on*, vol. 55, no. 5, pp. 1080–1086, 2007.

[87] G. A. Conway, S. L. Cotton, and W. G. Scanlon, "An antennas and propagation approach to improving physical layer performance in wireless body area networks," *Selected Areas in Communications, IEEE Journal on*, vol. 27, no. 1, pp. 27–36, 2009.

[88] D. Kurup, W. Joseph, G. Vermeeren, and L. Martens, "Path loss model for in-body communication in homogeneous human muscle tissue," *Electronics letters*, vol. 45, no. 9, pp. 453–454, 2009.

[89] ——, "In-body path loss model for homogeneous human tissues," *Electromagnetic Compatibility, IEEE Transactions on*, vol. 54, no. 3, pp. 556–564, 2012.

[90] G. Noetscher, S. N. Makarov, and N. Clow, "Modeling accuracy and features of body-area networks with out-of-body antennas at 402 mhz," *Antennas and Propagation Magazine, IEEE*, vol. 53, no. 4, pp. 118–143, 2011.

[91] S. K. Mitra and J. F. Kaiser, *Handbook for digital signal processing*. John Wiley & Sons, Inc., 1993.

[92] A. S. Glassner, *An introduction to ray tracing*. Morgan Kaufmann, 1989.

[93] K. S. Kunz and R. J. Luebbers, *The finite difference time domain method for electromagnetics*. CRC press, 1993.

[94] A. Taflove and S. C. Hagness, *Computational electrodynamics*. Artech house, 2005.

[95] SPEAG, "Speag publications."